Broad-Band Cavity Ring-Down Spectroscopy

Stephen M. Ball and Roderic L. Jones*

University Chemical Laboratory, Cambridge University, Lensfield Road, Cambridge, CB2 1EW, United Kingdom

Received April 7, 2003

Contents

Stephen Ball received his Bachelor's degree in Chemistry from Oxford University. He remained at Oxford where he received his D. Phil. degree in Chemistry having made measurements on the quantum yields of electronically excited oxygen atoms and oxygen molecules from the near-UV photolysis of ozone. Following a postdoctoral fellowship at the National Center for Atmospheric Research in Boulder, CO, he returned to the United Kingdom and Cambridge University, where he now holds an Advanced Research Fellowship funded by the Natural Environment Research Council. He is also the Chemistry Fellow of New Hall, Cambridge. His research interests lie predominately in the use cavity ring-down spectroscopy and related techniques to study the variability of atmospheric trace species.

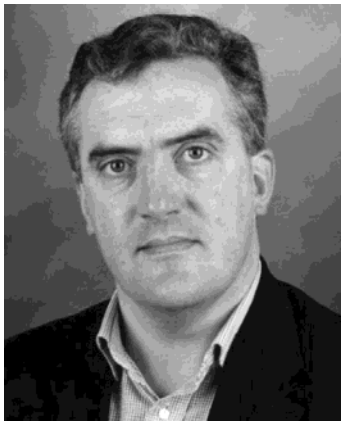

Rod Jones obtained his doctorate degree in Atmospheric Physics in the Department of Atmospheric Physics at the University of Oxford, where he was involved, with colleagues, in the measurement of upper atmosphere composition and structure from satellites. Following a move to the UK Meteorological Office in Bracknell, U.K., he became involved in observational studies of tropospheric chemistry using a C130 aircraft, where he was involved in the NASA/NOAA-led airborne missions to study ozone losses in both polar regions. In 1990 he obtained a Lectureship in the Department of Chemistry at Cambridge, where he has pioneered the development and use of novel instruments for atmospheric studies. He became a Reader in 1999 and is a Fellow of Queens' College Cambridge.

1. Introduction

The atmosphere is a complex mixture of interacting trace gases whose atmospheric residence times vary from less than one second up to many years depending on the molecule's reactivity.[1−3] Highly reactive radical species have the shortest atmospheric lifetimes and lowest ambient concentrations (typically parts per trillion), yet it is the chemical reactions of these molecules[4] that control the rates of processing and hence atmospheric lifetimes of natural and anthropogenic emissions. Owing to their short life-

10.1021/cr020523k CCC: $44.00
Published on Web 11/18/2003

times, the spatial and temporal distribution of atmospheric radicals is highly variable, leading in turn to highly variable rates in the chemical processing of emissions and the production of secondary pollutants. Indeed, it seems likely that a large fraction of the chemistry of the troposphere in particular occurs at the small scale, for example, at the interface between a pollution plume and the background air. To be able to form an understanding of these processes, measurements of short-lived atmospheric species[1,5] are required which are sensitive, unambiguously selective toward the target species, and acquired rapidly on a spatial scale sufficient to resolve the variability.

In the 15 years since its inception, cavity ring-down spectroscopy (CRDS) has established itself as a selective and sensitive method for making absorption measurements on weakly absorbing or highly dilute samples.[6−11] The detection of a wide range of species has been accomplished in the laboratory, and many of these species are of atmospheric importance. Moreover, the sensitivities demonstrated for the laboratory instruments are approaching the levels (and in certain cases are already sufficient) to probe species at the concentrations present in the atmosphere. Being an absorption technique, CRDS is also able to provide absolute measurements of an absorber's concentration provided that molecular absorption cross sections are known from laboratory measurements and the various contributions to the absorption spectrum of the sample mixture can be spectrally separated. Cavity ring-down techniques therefore offer an alternative to other methods of making absorption measurements in the atmosphere, of which long-path (∼10 km) differential optical absorption spectroscopy (DOAS) has previously been the most widely applied in the visible and UV regions of the electromagnetic spectrum.[12−14] However, compared to long-path DOAS, CRDS makes measurements on an intrinsically smaller spatial scale determined by the length of the optical cavity (typically one meter), and thus CRDS instruments have applications in the attribution of local sources/sinks and the investigation of small-scale chemical processing in the atmosphere.

This paper briefly reviews the use of absorption spectroscopy in atmospheric studies (section 2) concentrating on the visible and UV regions of the spectrum where many atmospherically important species have been probed via spectrally broad absorption bands arising from their electronic transitions. In atmospheric applications, absorption by the target species must be distinguished from overlapping absorptions due to other species and the ill-defined or unknown attenuation due to atmospheric aerosol. This is commonly achieved using DOAS methods to analyze spectra acquired across a wide range of wavelengths, the subject of section 3 of this review.

The underlying principles of CRDS are discussed in section 4, including where the latter technique is already being applied to atmospheric studies. The extension of CRDS to broad-band light sources and hence to DOAS analysis methods is developed in section 5, where the relatively few examples of such instruments reported in the literature before mid-2003 are reviewed in some depth. The procedure and apparatus required for a broad-band CRDS measurement are introduced, including the critical element for simultaneous time- and wavelength-resolved detection of the radiation leaking from the ring-down cavity: the use of a charge-coupled device (CCD) detector. The significant advantages of combining broad-band variants of CRDS with the established analysis methods of DOAS are highlighted from section 5 onward. Sections 6 and 7 explore existing and potential applications of broad-band CRDS and present examples to show how the concentrations of several atmospherically important target species are retrieved quantitatively from the measurements. Because the spectral fitting procedures are based on DOAS methods, they are able to retrieve the absorber amounts even where the broad-band spectra are complicated by the finite spectral resolution of the instrument, the presence of strong overlapping absorption features due to other absorbers, and extinction by atmospheric aerosol. Long path DOAS methods for atmospheric studies have employed light sources at visible and UV wavelengths, and inevitably this review of broad-band cavity ring-down spectroscopy also focuses on these regions of the spectrum. There is, however, no fundamental reason further technological developments should not extend the applicability of broad-band CRDS to other spectral regions, a subject explored further in section 8.

2. Atmospheric Absorption Spectroscopy in the Visible and UV Regions of the Spectrum

Spectroscopic methods, exploiting the unique interaction properties of different molecules with electromagnetic radiation, have been used extensively to measure the composition and structure of the Earth's atmosphere.[1,5,15,16] It is beyond the scope of this review to discuss these methods in detail, other than to indicate that spectroscopic measurements in the Earth's atmosphere have made use of absorption and thermal emission, have utilized most regions of the electromagnetic spectrum, and have exploited many different observing methodologies and platforms. The common feature of these techniques, however, is that the target molecules are identified unambiguously via their characteristic interaction with electromagnetic radiation, a process which in absorption spectroscopy generally also allows the concentrations of the absorbing species to be quantified absolutely.

This review focuses on measurement methodologies employing the subset of spectroscopic transitions that occur in the UV and visible regions of the electromagnetic spectrum. These are predominantly either electronic in origin, e.g., O_2,[17] O_3,[18−20] NO_2,[18,20,21] NO_3,[18,20,22−24] HONO,[18,20] HCHO,[18,20] BrO,[18,20] and IO,[18,20] or in some cases the vibration−rotation overtone absorptions of molecules whose fundamental absorption bands reside in the mid-infrared, e.g., H_2O.[17,25,26] At UV and visible wavelengths, the Planck function, and hence any thermal emission signal, is weak at typical terrestrial temperatures. In consequence, emission spectroscopy cannot, in

general, be exploited and absorption spectroscopy using either natural (e.g., solar, lunar etc.) or artificial sources must be used as a measurement method.

The absorption of electromagnetic radiation is governed by the Beer−Lambert law, which can be written in the form

$$trans(\lambda) = \frac{I(\lambda)}{I_0(\lambda)} = \exp[-\alpha(\lambda)l] = \exp[-\sum_i \sigma_i(\lambda)x_i l] \quad (1)$$

where the optical transmission at wavelength λ over an absorption path of length l is given by $I(\lambda)/I_0(\lambda)$, the ratio of the initial and final radiation fluxes. $\alpha(\lambda)$ is the absorbance per unit path and is composed of the absorption cross section $\sigma_i(\lambda)$ of absorber or scatterer i and its concentration x_i, the summation being performed over all absorbing or scattering species. The product $\alpha(\lambda) \times l$ is termed the optical depth. The ultimate sensitivity of a measurement of species i is determined by the accuracy to which the transmission can be measured, and this in turn depends on the measurement technique used, the absorption cross section of the molecule in question, the presence of other interfering absorbing species, and the absorption path length.

For stratospheric composition measurements from satellite and balloon platforms or ground-based instruments, absorption path lengths are determined by the observation geometries used and are generally hundreds of kilometers in the horizontal. In the infrared region of the spectrum, the pressure broadening of ro-vibrational transitions can be spectrally resolved and exploited in inversion methods,[27,28] but it is usually not possible to resolve any pressure broadening for transitions at UV and visible wavelengths. Hence, in general, only path-average measurements can be made, restricting the horizontal and vertical resolutions that are achievable.

In the troposphere, practical factors restrict absorption path lengths to a few kilometers, although the increased sensitivity arising from long absorption path lengths compared to those obtainable in the laboratory remains. The pioneering work of Platt and Perner and their co-workers led to the development of long-path differential optical absorption spectroscopy (DOAS), which has now been widely applied to measure surface and boundary layer concentrations of a range of species, for example, NO_2, NO_3, HONO, OH, O_3, HCHO, SO_2 (see refs 29−32 and a number of more recent reviews[12−14]). Some notable recent deployments of DOAS instruments have extended the measurements of NO_3[33−39] and have led to the detection of BrO,[40] IO,[41−43] and OIO.[44]

For the NO_3 molecule, measurements are made generally using its $B\,^2E' \leftarrow X\,^2A'_2$ electronic transition at 662 nm whose peak cross section[18,22−24] is around 2×10^{-17} cm^2 molecule^{-1}. The DOAS systems currently in use typically have path lengths of the order of 10 km[13,36,39,45] to achieve the sensitivity of ca. 1 pptv (parts per trillion by volume) necessary to probe NO_3 in the atmosphere. Such high sensitivities require that the optical density along the path be measured to an accuracy of 0.02%,[36] and more usually realized measurement accuracies would require correspondingly longer absorption path lengths to achieve the same sensitivity. As only path-averaged measurements are possible with the long-path DOAS method, this determines the spatial resolution achievable, although a DOAS approach for OH using a multipass cell has been reported.[46]

In the troposphere, and particularly in the planetary boundary layer with its highly localized emission sources, structure is expected to be present on spatial scales well below that observable with the typically used DOAS approaches. An in situ variant of the DOAS method is thus highly desirable. As described in this paper, such a method has in fact been realized by combining the DOAS approach with the ultrasensitive absorption method of cavity ring-down spectroscopy (CRDS). The CRDS technique provides absorption path lengths of many kilometers confined within a high-finesse optical cavity of the order of 1 meter baseline length and thus is capable of making measurements similar in sensitivity to DOAS but on a vastly reduced spatial scale. However, the majority of CRDS applications demonstrated in the laboratory to date have used essentially monochromatic laser radiation, losing an important advantage of the DOAS method. Indeed, the major subject of this review—combining the sensitivity of CRDS and the selectivity of the DOAS technologies for field studies—arises from the use of a broad-band source and a wavelength-resolved photodetector. Greatest flexibility is obtained when the photodetector is two-dimensional and thus able to follow simultaneously the time dependence of each wavelength-resolved channel. The use of (essentially monochromatic) lasers and broad-band light sources in CRDS is reviewed in sections 4 and 5, respectively, but first we provide a brief review of the DOAS methodology, which in later sections is applied to the analysis of broad-band CRDS spectra.

3. Differential Optical Absorption Spectroscopy (DOAS)

Application of the Beer−Lambert law (eq 1) is straightforward under laboratory conditions where $I(\lambda)$ and $I_0(\lambda)$ can be measured directly and where the measurement wavelength can be selected to be one at which only the species of interest absorbs. However, determination of the target species' optical depth is far more complex in the atmosphere, where the absorptions of several interfering molecules may overlap at the measurement wavelength and where broad-band extinction due to Rayleigh and Mie aerosol scattering are significant. In this case, the unambiguous identification of an individual species is still often possible through the use of spectral oversampling, where the atmospheric absorption is measured across a broad spectral bandwidth (typically 20−100 nm) at hundreds of wavelengths. Molecules that possess structured absorptions on scales within this bandwidth can be distinguished from any underlying scattering terms in the optical depth which generally vary relatively smoothly with wavelength and can thus be removed by an appropriate high-pass filtering method. In addition, the absorp-

tions due to several different constituents can be measured simultaneously by appropriate optimal fitting of the relevant molecular absorption cross sections to the observed spectrum, the use of absorptions measured simultaneously at many wavelengths making the problem overdetermined.

The spectral fitting process of a generalized active DOAS-type measurement is illustrated in Figure 1 for two hypothetical species A and B whose structured absorption spectra overlap in the region of interest (see part A). The first step is to measure an observed spectrum $I(\lambda)$ and a reference spectrum $I_0(\lambda)$ where the latter is readily obtained by directly recording the spectrum of the light source with the same detection system. Alternatively, $I_0(\lambda)$ can be obtained from an atmospheric spectrum recorded under conditions when known amounts of the absorbing species are present between the source and detector. The latter is used in passive techniques (e.g., zenith sky spectroscopy[33,34]) because $I_0(\lambda)$, the unattenuated extraterrestrial spectrum, cannot easily be measured directly. Part B of Figure 1 shows the simulated $I(\lambda)$ and $I_0(\lambda)$ used in the present example, where $I_0(\lambda)$ is the wavelength-dependent source spectrum including the response function of the instrument's detector and $I(\lambda)$ is the observed spectrum which includes contributions due to absorption by molecular species A and B and the effects of an unstructured but varying absorption characteristic of Rayleigh or Mie aerosol scattering. Part B of Figure 1 shows the Rayleigh or Mie extinction as the dot−dashed line. Statistically generated noise representing photon shot noise has been added to the simulation of the observed spectrum.

The next step in the DOAS analysis is to calculate the optical depth over the absorption path from the natural logarithm of the ratio of the reference and observed spectra

$$OD(\lambda) = -\ln\left[\frac{I(\lambda)}{I_0(\lambda)}\right] = \sum_i \sigma_i(\lambda) x_i l \qquad (2)$$

where the summation includes all absorbing and scattering species present in that spectral region. The smoothly varying scattering terms are then removed from the optical depth through the use of a high-pass filter. A variety of filtering methods have been employed,[12−14] but the simplest and most commonly implemented involves the use of a polynomial which is fitted to the measured optical depth and then subtracted from it, leaving the so-called differential spectrum or differential optical depth, $\Delta OD(\lambda)$

$$\Delta OD(\lambda) = \sum_i \sigma_i(\lambda) x_i l - P(\lambda, n) \qquad (3)$$

where $P(\lambda,n)$ is the polynomial in λ of order n fitted to the observed optical depth. The resulting differential optical depth (taking $n = 2$) for the simulation is shown as the gray line in part C of Figure 1, discussed below. The process of high-pass filtering illustrated above enables the DOAS method to largely overcome the problems arising from unknown or inadequately characterized atmospheric absorption or scattering. However, it should be recognized that the rejection of less structured contributions to the measured absorption is a function of the specific filter used, and therefore it is necessary to exercise care when applying a filter to prevent inadvertent rejection or smoothing of differential structure due to the

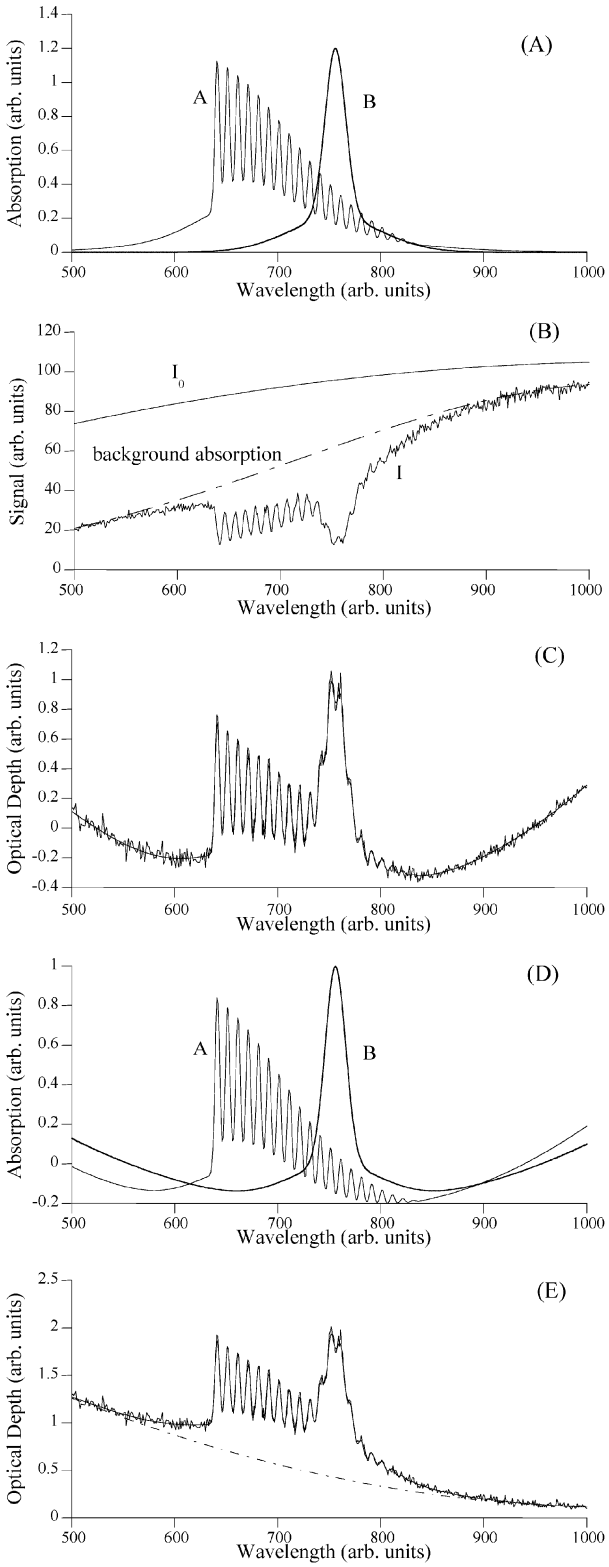

Figure 1. Schematic illustration of the principles of the DOAS method, in this case for a smoothly varying underlying absorption and two idealized species A and B, indicative of H_2O and NO_3 absorptions (see section 3). Details of the various panels are given in the text.

molecular absorbers. There are a variety of more sophisticated methods including Fourier transform filtering methods and orthogonalization of the various differential cross sections fitted, but the basic approach remains unchanged.

Differential cross sections for each of the species that are to be fitted to the measurement are then obtained by filtering the molecular absorption cross sections available from laboratory measurements and complied in standard spectral databases.[17,18,20,26] The same filter parameters applied in the calculation of the measured differential optical depth (here, the order of the polynomial n and the wavelength range) must also be used for determining the differential cross sections

$$\Delta\sigma_i(\lambda) = \sigma_i(\lambda) - P'_i(\lambda,n) \quad (4)$$

where i designates the absorbing or scattering species (in this example, i = A or B). The differential cross sections for species A and B are shown part D of Figure 1. The path-integrated concentrations of each species are deduced by simultaneously fitting the derived differential cross sections to the measured differential optical depth using an appropriate minimization method. The result is shown as the solid curve overlaid on the "measurement" in part C of Figure 1. With the path-integrated concentrations of absorbers A and B now known, the underlying absorption/extinction can be retrieved by subtraction of the fitted molecular spectra from the measured spectrum in absolute absorption units. The fitted optical depth (due to the sum of the molecular absorbers and the aerosol continuum) is compared with the measurement in part E, the solid black and underlying gray curves, respectively. Typically, the differential spectrum is recorded at several hundred wavelength points and the number of fitted parameters is generally less than 10. Thus, the problem is greatly overdetermined and can usually be solved with a nonlinear least-squares method.[47]

It is usual to match the instrument resolution to the molecular absorption of interest so that the Beer−Lambert law can be taken to hold. In this case, if the absolute absorption cross sections are known, the path-integrated amounts of each absorbing species may then be derived via the DOAS analysis by direct comparison with the known cross section. However, as discussed in detail below, for highly structured absorbers such as H_2O and O_2, significant non-Beer−Lambert law behavior can be observed and more sophisticated analysis methods are required.[48]

4. Cavity Ringdown Spectroscopy

O'Keefe and Deacon[49] are widely acknowledged as being the first to demonstrate cavity ring-down spectroscopy (CRDS) when in 1988 they recorded the CRDS spectrum of vibrational overtones of the b $^1\Sigma_g^+ \leftarrow$ X $^3\Sigma_g^-$ transitions of molecular oxygen in air. Since then, cavity ring-down spectroscopy has become well established in many research laboratories as a method of making sensitive and quantitative measurements of the absorptions of a large number of weakly absorbing or highly dilute gas-phase species. The technique is now finding applications in the liquid phase,[50−52] for studies of solid films,[53−56] and for measuring atmospheric particles[57,58] and soot.[59] A review of the various ways in which CRDS has been incorporated into experimental methodologies is beyond the scope of this paper, especially since many excellent reviews of the technique already exist.[6−11] In particular, the review by Berden et al.[9] provides a comprehensive tabulation of species that have been probed in this way prior to June 2000, a great many being of interest to atmospheric science. Brown's review[11] of CRDS in this special issue updates and extends the list for atmospheric trace gases and aerosol particles. Instead, this paper focuses on a subset of the various CRDS techniques—those that use broad-band radiation to acquire spectra over a wide range of wavelengths simultaneously—and especially the application of such methods to absorption measurements of atmospheric samples. However, before these are discussed, it is pertinent to review briefly the fundamental theory of CRDS.

4.1. Ringdown Decay

In its simplest form, the technique of CRDS relies on injecting monochromatic radiation from a pulsed laser into a high-finesse cavity composed of highly reflective mirrors. A detector such as a photomultiplier tube or an avalanche photodiode observes the rate of decay of the light intensity leaking from the cavity's output mirror. Where the spectral width of the laser radiation is sufficiently narrow to excite only a single Fabry−Perot mode of the cavity, it has been shown that the intensity decay is characterized by a single-exponential function.[60] For an empty (i.e., evacuated) cavity formed by two identical mirrors, the 1/e decay time constant of the exponential, τ, commonly called the ring-down time, is given

$$\tau(\lambda) = \frac{d}{c\,|\ln R(\lambda)|} \quad (5)$$

where d is the mirror separation, $R(\lambda)$ is the geometric mean reflectivity of the cavity's mirrors, and c is the speed of light. Note that the mirror reflectivity and hence the empty cavity ring-down time depends on wavelength.

Radiation obtained from pulsed laser systems is not strictly monochromatic but usually extends over several neighboring Fabry−Perot modes of the cavity. Beating between these modes can lead to oscillations in the intensity of the cavity output during an individual decay.[61] However, the practical effects of this are small if the experiment is conducted in such a way that many cavity modes are excited[62]—a so-called "quasi-continuum of modes"—and a number of decay signals are averaged together before fitting for the ring-down time. Nevertheless, this represents a compromise and the ultimate sensitivity of the CRDS technique can only be realized if precautions are taken to match the laser radiation to a single Fabry−Perot mode of the cavity. For example, van Zee et al.[63] demonstrated a pulsed single-mode instrument having a fractional uncertainty of 0.03% in the fitted ring-down time for an individual decay, compared to a typical uncertainty of 1% in multimode systems.

Continuous wave (CW) sources, external cavity diode lasers (ECDL) being the most commonly employed, have inherently narrower bandwidths than pulsed sources, and thus CRDS systems based on CW sources[64−69] seldom suffer from multimode phenomena. The issue instead is that the frequency of the laser is no longer guaranteed to overlap with a mode of the ring-down cavity. Excitation of the cavity therefore relies on accidental resonance between the laser and the cavity, and modulation of the laser frequency or the cavity length is usually employed to ensure such overlap happens at least once during the modulation period. Whenever the laser and cavity come into resonance, light intensity propagates through the cavity onto the photodetector. It is usual to arrange that the laser beam be interrupted once the detector registers a signal above a certain threshold, for example, using an acousto-optic modulator. The subsequent ring-down decay is then recorded in the usual fashion. Schemes also exist where the intensity of light exiting the cavity is used in a feedback loop to actively lock the cavity into resonance with the CW laser source, and these instruments show exceptional sensitivity.[70,71] Another alternative is to use a cavity with a dense mode structure and scan the CW laser slowly in wavelength while recording the steady-state light intensity coming from the cavity. The technique is called cavity-enhanced absorption spectroscopy (CEAS)[72] or CW−integrated cavity output spectroscopy (ICOS).[73] This technique is the most simply implemented of the CW methods but requires an independent measurement of the wavelength-dependent mirror reflectivity (or the absorption of a calibration sample) in order for its relative measure of the absorbance to be made quantitative.

4.2. Quantitative Absorption Measurements by CRDS

The bandwidth of the source radiation has further implications when CRDS is employed to record the absorption spectra of samples within the cavity.[60] Provided that the spectral width of the probe radiation is much narrower than that of the absorption feature, the intensity of light leaking from the cavity also decays exponentially with a ring-down time $\tau'(\lambda)$ that is directly related to the ring-down time of the empty cavity and the attenuation due to the sample

$$\frac{1}{\tau'(\lambda)} = \frac{1}{\tau(\lambda)} + c\alpha(\lambda) = \frac{1}{\tau(\lambda)} + c\sum_i \sigma_i(\lambda)x_i \qquad (6)$$

where c is the speed of light and the remaining quantities have the same meaning as in the Beer−Lambert law expression of eq 1. The condition that the probe radiation be narrower than the absorption feature is easily satisfied for lasers such as ECDLs used in CW CRDS, though it is still necessary to ensure that the laser and the cavity come into resonance sufficiently often during a scan across an absorption line to reproduce its proper line shape. More care must be exercised when using pulsed laser systems because their bandwidths are often comparable to the width of a molecule's Doppler and pressure broadened lines potentially giving rise to decays which are no longer simple exponential in form (see sections 5 and 6). At least the quasi-continuum of modes excited in the ring-down cavity of a pulsed system ensures that many cavity modes sample the molecular absorption feature at any given wavelength.

Ringdown times are measured in absolute units of seconds, and digitizers such as those used in digital storage oscilloscopes are able to monitor on a highly accurate time base the decaying signals from which values of the ring-down times are subsequently extracted by computer fitting of an exponential function. In laboratory experiments, the wavelength of the probe laser is usually scanned across the spectral feature of interest and the CRDS absorption spectrum is constructed by comparing the ring-down times with those measured for a scan with the absorber excluded from the cavity (see eq 6). Thus, like conventional absorption spectroscopy, CRDS can be configured to provide *absolute* measurements of concentrations. However, for samples that are mixtures, absolute concentration measurements are only achievable if the wavelength-dependent losses by mechanisms other than absorption by the target species are also known, i.e., all the other terms contributing to the summation in eq 6. In the atmosphere, these could, like the target molecule itself, be highly variable, e.g., scattering by aerosol particles or variation in the concentration of an overlapping gas phase absorber. Thus, even if the laser has sufficient tunability, it is unlikely to be practical to obtain scans over the extended spectral ranges typically used in DOAS field instruments to measure molecules with broad absorption features at visible and near-UV wavelengths.

Different strategies are employed instead. A target species can be monitored by acquiring ring-down times at carefully selected wavelengths by modulation of the radiation between two wavelengths, the peak and far wings of the molecule's absorption band, in both cases being careful to avoid wavelengths where other species absorb. The absorber amount is deduced from the variation in the ring-down times on- and off-resonance and the difference in the molecular absorption cross section including any correction required to account for a change in mirror reflectivity (though the potential remains for interference by variable aerosol scattering). Field instruments based on tunable diode laser absorption spectroscopy (TDLAS) already use a related methodology to obtain scans over a selected resolved ro-vibrational transition of the target molecule, and it is likely that future CW−CRDS field instruments based on ECDLs will follow a similar strategy (though see the exception of ref 69 discussed in section 4.3).

Another approach is to measure the ring-down time at a single wavelength at the peak of an absorption band while modulating the concentration of the target species, thereby side-stepping issues concerned with the wavelength dependencies of any interferences. This method necessitates the rapid and selective removal of the target species from the sample

flow without affecting the remaining constituents or creating others that might contribute to absorption or scattering at the single probe wavelength. As such, this method must be carefully tailored to a specific application, and measurements have been performed with great success on NO_3 at 662 nm, modulating its concentration by titration with NO, the reaction selectively removing NO_3 during its residence time ($\approx$1 s) in the inlets of the instruments.[69,74−76] The photolytic removal of NO_3 from the sample has also been proposed.[77]

For studies in the atmosphere, the advantage of the above spectral or chemical modulation methodologies is that measurements are obtained more frequently than would be possible when scanning across the whole absorption spectrum, thereby allowing the concentration of rapidly varying species to be recorded. The disadvantage is that the absorber amount is deduced from just two pieces of information, which requires a foreknowledge of the potential spectral or (photo)chemical interferences. Yet the form of eq 6 suggests that where CRDS spectra are obtained using a broad-band light source, the contribution from the various absorbers to the spectrum can be separated via DOAS methods using their known absorption cross sections and any aerosol scattering/absorption can be removed by spectral stripping. Furthermore, the broad-band measurements collect spectral information across the whole absorption band simultaneously—in principle, in a single laser shot—and thus are also able to monitor rapidly changing concentrations. Cavity ring-down spectroscopy using broad-band light sources, the main subject of this review, is discussed extensively from section 5 onward.

4.3. Cavity Ringdown Spectroscopy for Atmospheric Studies

The high sensitivity demonstrated for laboratory-based CRDS instruments (even multimode, where the minimum detectable absorbance[9] is from 10^{-6} to 10^{-10} cm^{-1}) is attractive to those seeking to make measurements of highly dilute absorbers—atmospheric trace species in the case of the present authors. The technique has become so widely implemented in laboratory-based research that CRDS mirrors are now commercially available with reflectivities of >99.99% throughout the visible region of the spectrum and at certain wavelengths into the near-infrared. Reflectivities in the near UV are at present only a little less efficient. Thus, a compact (<1 m) instrument can provide access to ring-down times equal to many tens of microseconds for the empty cavity (eq 5), equivalent to path lengths of 10 km or more. These path lengths are comparable to those employed by conventional long-path DOAS instruments, although now the cavity length determines the vastly smaller intrinsic spatial scale of the CRDS measurement.

A large fraction of laboratory-based CRDS instruments operating at visible and near-UV wavelengths detect species that are also of atmospheric importance, some recent examples being NO_2,[68,78−81] NO_3,[77,82] HONO,[83] H_2O,[67,84] OH,[62,85−87] BrO,[88,89] IO,[90,91] and OIO.[92] Some of the above papers report the first proof-of-principle experiments en route to construction of a field instrument, while other authors with no such ambitions nevertheless refer to the potential applications of their studies for atmospheric measurements. Moreover, all of the species in the above list have been detected in the atmosphere by DOAS (see section 3) and hence can be considered as candidates for broad-band cavity ring-down studies. So far, only NO_2[79] and NO_3[82] from the above list have been probed in this way: the other broad-band experiments in the scientific literature and the species probed by them are reviewed in section 5.

Given the efforts of so many investigators, it is surprising that the literature contains few reports of measurements made by CRDS in the field (as opposed to measurements, like the original cavity ring-down demonstration,[49] made in the laboratory on a controlled atmosphere). NO_3 is currently the molecule of main interest, with three groups having constructed prototype instruments. Brown et al.[74−76,93] are the most advanced, having reported atmospheric measurements made via the chemical modulation of NO_3. The ring-down times measured at the peak of the 662 nm absorption band (and hence also the sensitivity of their instrument) were increased through the use of Teflon filters to remove aerosol from the sample. This had the added benefit of decoupling variations in τ(662 nm) from variations in atmospheric aerosol, the drawback of the approach being that the Teflon filters needed to be changed periodically. The instrument also provided the first in situ measurements of atmospheric N_2O_5, this species being the reservoir of atmospheric NO_3. The N_2O_5 measurements were achieved by directing 50% of the laser output through a second identical ring-down cavity heated to 80 °C in which ambient N_2O_5 was thermally decomposed to NO_3 and the latter measured in the same way. The sensitivity of the instrument was 0.25 pptv (1σ) for both NO_3 and N_2O_5 in a 5 s integration period.

Very recently, Simpson[69] reported measurements of N_2O_5 performed in December 2002 and January 2003 at the University of Alaska in Fairbanks, AK, where ambient conditions meant that the temperature-dependent equilibrium between NO_3 and N_2O_5 overwhelmingly favored the latter. The instrument's mode of operation shared several common features with the Brown et al. instrument. N_2O_5 was monitored via measurements of NO_3 formed from its thermal decomposition in a heated inlet. The amount of NO_3 in the cavity was similarly quantified by measuring ring-down times at a single fixed wavelength at the peak of the molecule's 662 nm absorption band while modulating its concentration by the chemical reaction with NO. Again, the value of the ring-down time and the reproducibility of the measurements were increased by drawing ambient air into the instrument through a Teflon filter. However the light source was different: the instrument, which was based on the prototype of King et al.,[77] employed an external cavity diode laser. The use of an ECDL meant that the instrument was lightweight, compact, and consumed a modest amount of electrical power.

The detection limits demonstrated for the instrument were 2.4 pptv for N_2O_5 and 1.7 pptv for NO_3 (both 2σ limits for a 25s integration), only slightly poorer than those of Brown's instrument, which has a 50% longer baseline ring-down time.

Ball et al.[82] took a very different approach, using a broad-band dye laser source and a two-dimensional CCD detector. This instrument is discussed further in section 5.2.2, and representative spectra of laboratory samples of oxygen and NO_3 are shown to aid the discussion in sections 6 and 7. The resulting broad-band absorption spectra were analyzed using the DOAS methodology discussed in section 3, giving an NO_3 sensitivity of 0.5 pptv for laboratory samples (150 s integration time). The sensitivity was reduced to $\approx$2 pptv for ambient samples due largely to the reduction in the ring-down times caused by aerosol extinction (up to 1×10^{-6} cm^{-1}), the values of which were also quantified by the DOAS analysis. Although the results have yet to be published, this instrument has been deployed to measure atmospheric NO_3 and OIO at Mace Head (Eire) during the North Atlantic Marine Boundary Layer Experiment. To our knowledge, this is the first occasion that broad-band cavity ring-down spectroscopy has been taken into the field.

5. Cavity Ringdown Spectroscopy with Broad-Band Light Sources

It is interesting to note that, but for the few examples highlighted in the following sections, practitioners of CRDS have deliberately sought to avoid the use of spectrally broad radiation sources. For example, Romanini and Lehmann[94] used an elevated pressure of HCN to ensure that the width of its rotationally resolved transitions were broader than the 0.18 cm^{-1} line width of the probe laser. In their study of the spectroscopy of molecular oxygen near 1.27 μm (pressure and Doppler broadened line width of 0.098 cm^{-1}), Newman et al.[95] confined the analysis of the ring-down signals to just the early part of the decay where the effects due to the broader line width of their laser (0.25 cm^{-1}) were minimized. These investigators considered it necessary to take such precautions because complications occur in CRDS when the spectral width of the probe radiation is similar to or wider than that of the molecular absorption feature.[60,61,85] Specifically, the ring-down decays cannot satisfactorily be described by a single-exponential function and hence attributed a unique ring-down time—the decays are termed "multiexponential". In turn, an attempt to fit a 1/e decay time to a multiexponential ring-down event and then use eq 6 to calculate an absorber amount would result in the underestimation of the absorber's true concentration (see section 6).

Notwithstanding the above discussion, analytical treatment of multiexponential decays *is* readily tractable and importantly still yields quantitative measurements of absorber amounts provided that the spectral distribution of the radiation contributing to the ring-down event is known.[60] The primary disadvantage of broad-band compared to narrow-band studies and the reason for the increased complexity of the analysis is that the light source no longer determines the spectral resolution of the measurement, hence the likelihood of multiexponential ring-down decays must be explicitly incorporated into the analysis procedure. However, the greater advantage of using spectrally broad sources for atmospheric studies is that, because information is collected simultaneously over a wide range of wavelengths, the DOAS methodology can be applied to fit the overlapping absorptions contributing to the broad-band CRDS spectrum including ill-defined aerosol absorption/scattering terms. The retrieval of absorber amounts from the analysis of CRDS spectra obtained with broad-band sources seems still to be in its infancy (an easily implemented retrieval method is discussed in some detail in sections 6.2 and 6.3). Nevertheless, we hope to demonstrate in this review that for atmospheric studies the disadvantages of the increased complexity of the analysis method are outweighed by the advantages afforded by the DOAS methodology, especially when applied to the simultaneous detection of time- and wavelength-dependent ring-down signals.

The literature contains only a few reports by investigators who have employed truly broad-band sources in their CRDS studies. Table 1 summarizes these studies in order of publication date. The criterion for inclusion in Table 1 is that the bandwidth of the radiation source is at least an order of magnitude greater than the width of the molecular absorption features (so the studies referred to above[94,95] do not qualify). Several of the broad-band studies sought to avoid the issue of multiexponential decays altogether by reducing the dimensionality of the experiment by *either* detecting time-dependent signals restricted to a narrow range or subset of wavelengths *or* detecting time integrated or time-gated signals dispersed in wavelength. These "one-dimensional" studies are reviewed in section 5.1. In contrast, section 5.2 reviews two related versions of broad-band CRDS that used a two-dimensional detector to resolve the radiation exiting the ring-down cavity in both time and wavelength simultaneously. This latter approach retains a major advantage of conventional CRDS, namely, that the measurements are independent of intensity fluctuations in the output of the light source.

5.1. One-Dimensional Broad-Band Cavity Ringdown Techniques

5.1.1. Fourier Transform Techniques

Engeln and Meijer[96] injected the output of a broad-band dye laser (400 cm^{-1} width centered at 763 nm) into a CRDS cavity and employed a Fourier transform spectrometer to select a subset of wavelengths from the cavity output. The temporal evolution of resulting multiexponential signal was recorded by a photomultiplier tube as a function of the displacement of the interferometer's mirror. This apparatus was thus an example of the type shown in Figure 2a, where part of the cavity output is selected before being directed onto a time-resolved, wavelength-integrating detector. After a number of hours of acquisition at some 3000 discrete mirror displace-

Table 1. Summary of Literature Reports of Cavity Ringdown Instruments Using Broad-Band Light Sources

technique	light source	central wavelength	bandwidth of light source	spectral width of measurement	detector	acquisition time of spectra	molecule	sensitivity per cm
Fourier transform cavity ring-down spectroscopy [96]	Nd:YAG pumped dye laser with grating in zero order (50 Hz)	763 nm	400 cm^{-1}	760.5−767.7 nm	Fourier transform spectrometer prior to PMT	4 h (200 decays at each of 3260 mirror positions) [a]	oxygen	2.5×10^{-7}
Ring-down spectral photography[101]	Nd:YAG pumped dye laser (20 Hz)	625−645 nm	<0.1 cm^{-1} [b]	narrow band (steps of 1 nm)[b]	time-dependent cavity output dispersed by rotating mirror and imaged onto CCD	not given (single shot measurement at 21 sequential wavelengths)[a]	propane	2×10^{-8} (single wavelength)
Pulse-stacked cavity ringdown spectroscopy[99]	free electron laser (11.8 MHz)	5.38 μm	25 nm	0.03 nm limited by resolution of monochromator	monochromator and liquid nitrogen-cooled HgCdTe detector	not given[a]	water vapor	2×10^{-9}
Cavity ringdown spectrography[79]	Nd:YAG pumped broadband dye laser	420 nm	25 nm	415−433 nm	spectrograph and CCD camera with image intensifier gated at consecutive time delays	not given	NO_2	1×10^{-5} [c]
Broad-band cavity ringdown spectroscopy[82]	Nd:YAG pumped broad-band dye laser (20 Hz)	660 nm	30 nm	650−670 nm	spectrograph (0.45 nm resolution) and clocked CCD camera	12 min	NO_3	4.7×10^{-9}
Broad-band ring-down spectral photography[102]	Nd:YAG pumped broadband dye laser	(i) 630 nm	>15 nm	(i) 625−641 nm	cavity output dispersed in time by a rotating mirror and in wavelength by a diffraction grating (1.5 cm^{-1} resolution),	single shot	(i) propane	(i) 2×10^{-8} at 636 nm
		(ii) 690 nm		(ii) 686−695 nm	then imaged onto CCD		(ii) oxygen	(ii) not given
Cavity ring-down spectroscopy of thin films[56]	Ti:Al_2O_5 & optical parametric amplifier (1 kHz) with difference frequency mixing	1500 cm^{-1}	15 cm^{-1}	1.5 cm^{-1} limited by resolution of spectrometer	spectrometer and liquid nitrogen-cooled HgCdTe detector	not given (100 s per spectral point; typically 41 points per spectrum)[a]	C_{60} film on BaF_2 substrate	1.3×10^{-7} per pass of sample
Fourier transform phase shift cavity ringdown spectroscopy[97]	xenon arc lamp (CW) modulated in intensity (100 kHz)	white light source	white light source	763.4−766.6 nm	Fourier transform spectrometer (resolution 0.5 cm^{-1}) and PMT	not given (5 recordings of in- & out-of-phase interferograms at 2000 mirror positions)[a]	oxygen	not given but better than 1×10^{-6} [c]
Incoherent broad-band cavity-enhanced absorption spectroscopy[100]	xenon arc lamp (CW)	white light source	white light source	(i) 627.7−630.3 nm	monochromator and diode array; resolution is (i) 0.026 nm and (ii) 1.2 nm	(i) 25 s or 500 s	(i) oxygen	not given but better than 1×10^{-7} for oxygen[c]
				(ii) 628−670 nm		(ii) 90 s	(ii) azulene	
Broad-band cavity ringdown spectroscopy, this work	Nd:YAG pumped broadband dye laser (20 Hz)	(i) 690 nm	30 nm	(i) 686−692 nm	spectrograph and clocked CCD camera; resolution is (i) 0.1 nm fwhm	(i) 150 s	(i) oxygen	(i) 6.3×10^{-9}
		(ii) 660 nm		(ii) 650−670 nm	and (ii) 0.2 nm fwhm	(ii) 130 s	(ii) NO_3 and water vapor	(ii) 1.2×10^{-9}

[a] The acquisition time was determined largely by the scan rate of the monochromator/spectrometer or the laser. [b] Although this proof-of-principle investigation was performed with a narrow-band laser, the potential for use of a broad-band source was discussed at length and demonstrated in later experiments. [c] Sensitivity estimated from data given in the report. Where insufficient data was given, an order of magnitude estimate of the sensitivity is made from the quality of the published spectra.

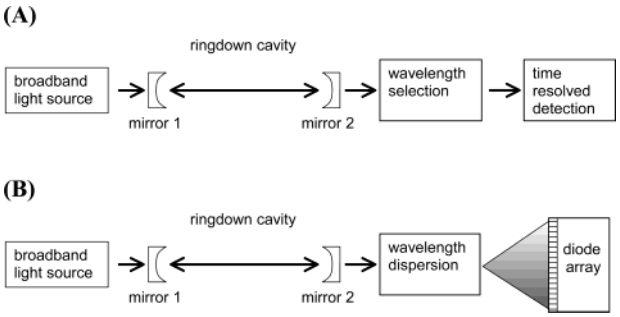

Figure 2. Schematic diagrams of one-dimensional broad-band cavity ring-down techniques. (A) Time-dependent detection of ring-down signals due to a preselected subset of wavelengths. (B) Time-integrated or time-gated detection of ring-down signals dispersed in wavelength.

ments, the complete data set was rearranged into arrays having the same time bin but different mirror displacement. The arrays were then Fourier transformed to yield time-dependent spectral intensity distributions. Ringdown times and thus an absorption spectrum of molecular oxygen were extracted from fits to data points of the same wavelength drawn from sequential time-dependent spectra. In terms of the radiation employed, this Fourier transform CRDS method is unquestionably a broad-band technique. However, the method does not provide simultaneous measurement of the cavity output in *both* time and wavelength because the data from which the ring-down decays are composed were collected at sequential mirror positions. In fact, the acquisition time of the full spectrum (4 h) is currently too long for monitoring short-lived atmospheric radicals, and it is likely that measurements of longer-lived species by this method would be compromised by variations in other absorption terms (e.g., aerosol scattering).

In a separate paper, one of the original authors and his colleagues[97] report an extension of the methodology in which a Michelson interferometer was placed before the ring-down cavity and used to preselect the frequencies of radiation entering the cavity. This too is a variant on the generic apparatus depicted in Figure 2a, except here the wavelength-dependent selection of the radiation is performed earlier in the optical train. In addition, the intensity of the light source was modulated and the phase shift in the output of the ring-down cavity monitored using a photomultiplier tube. Again, it was necessary to acquire data at a number of mirror positions (approximately 2000) before a complete spectrum of the sample could be obtained. The experiment is thus an analogue of phase shift cavity ring-down spectroscopy[98] using broad-band radiation to record, in this instance, a 3.5 nm section of b $^1\Sigma_g^+$ ($v' = 0$) ← X $^3\Sigma_g^-$ ($v'' = 0$) band of molecular oxygen near 765 nm. The especially exciting development in this work is the white light source: a Xe arc lamp, which produced incoherent radiation over a very wide spectral range.

5.1.2. Wavelength-Selected Techniques

A second approach was adopted by Crosson et al.[99] who used pulses from a free electron laser (25 nm fwhm centered at 5.38 μm) to record an absorption spectrum of water vapor. To avoid multiexponential decays, a monochromator was required to resolve the cavity output into separate narrow (0.03 nm) wavelength ranges incident sequentially on a single HgCdTe detector. The ring-down decays were thus recorded in a time-resolved manner, integrated in wavelength over the narrow range transmitted by the monochromator (see Figure 2a). Marcus and Schwettman[56] used the same strategy in their study of the mid-infrared absorptions of thin films of C_{60}. The radiation generated by frequency mixing using a seeded Ti:Al_2O_3 regenerative amplifier and optical parametric amplifier laser system was tunable in the range 1000−3300 cm^{-1} and had a bandwidth of ≈15 cm^{-1}. A portion of the radiation transmitted through the ring-down cavity was selected by a spectrometer (resolution 1.5 cm^{-1}) and detected in a time-resolved manner by a single HgCdTe detector. Again, the sample's spectrum was built up from a series of ring-down decays recorded at discrete steps of the spectrometer with the occasional retune of the laser frequency.

Both experiments discussed above[56,99] are effectively narrow-band CRDS where the monochromator/spectrometer (not the light source) determines the wavelength and bandwidth of the measurement. Indeed, neither group was attempting broad-band detection; rather they were seeking to demonstrate other aspects of CRDS (pulse stacking to increase the cavity transmission[99] or CRDS on thin films[56]) with lasers sources that were spectrally broad for unrelated reasons. While the above approach avoids multiexponential ring-down decays, it is however fundamentally inefficient in terms of making full use of the intensity emitted by the light source because output at wavelengths outside the range selected by the dispersive element is excluded from the detector.

5.1.3. Spectrally Resolved Techniques

Czyzewski et al.[79] demonstrated cavity ring-down spectrography using broad-band radiation from a Nd:YAG pumped dye laser. Broad-band radiation around 420 nm (15 nm fwhm) was passed through the ring-down cavity and dispersed in wavelength by a spectrograph. The wavelength-resolved spectrum of the cavity output was detected at a well-defined delay with respect to the laser pulse using a charge-coupled device (CCD) with a gated image intensifier. The gate width was typically 50 ns. This apparatus is an example of the type shown in Figure 2b, where the full bandwidth of the light source is used for each measurement. However, the gating of the image intensifier permitted a wavelength-resolved spectrum to be acquired at just one time delay within the ring-down event. Thus, Czyzewski et al. built up the temporal evolution of the cavity output over a number of laser shots by acquiring wavelength-resolved spectra for consecutively gate delays. Only once this process was complete could ring-down times be extracted from the data set. Even then consecutive data points along the decay trace derived from different laser shots, meaning that shot-to-shot variations in the laser output added noise to the decay and hence uncertainty to the fitted ring-down time.

Consequently, cavity ring-down spectrography in its present incarnation has lost one of the great advantages of cavity ring-down spectroscopy, namely, that the time constant of the ring-down transient is insensitive to intensity fluctuations of the laser.

Czyzewski et al. demonstrated their technique on a sample of 0.01 Torr of NO_2 (a mixing ratio of approximately 10 ppmv). The relative uncertainty quoted for the determination of the sample's absorbance was about 5%, which, assuming an average absorption cross section of 6×10^{-19} cm^2 molecule^{-1} for NO_2 in the region 415−433 nm,[21] equates to a sensitivity of approximately 1×10^{-5} cm^{-1}. This is modest by comparison with other narrow-band CRDS measurements of NO_2 [68,78,80,81] and is largely attributable to the relatively low reflectivity of the cavity mirrors (99.8% at 410 nm decreasing to 99.0% at 440 nm).

Incoherent broad-band cavity-enhanced absorption spectroscopy (IBBCEAS)[100] is the broad-band CRDS application most closely analogous to long-path DOAS. This is another example of the type of experiment shown in Figure 2b. Here, the cavity was illuminated by light from a continuous wave (CW) xenon arc lamp—an incoherent light source frequently employed in DOAS systems. In effect, the large paths traveled through the sample while the photons were confined to the cavity substituted for the extended optical path of the DOAS instrument. Photons leaking from the cavity were dispersed in wavelength by a monochromator and imaged by a diode array in much the same way as the return signal from a DOAS retro-reflector would be processed. The resulting time-averaged spectrum of intensity versus wavelength was, subject to certain caveats, used together with a similar spectrum obtained for an empty cavity (i.e., purged with a nonabsorbing gas) to obtain the wavelength-resolved absorbance of the sample. Indeed, in their paper, Fielder et al. show broad-band absorption spectra of oxygen and azulene obtained in the laboratory with sensitivities substantially better than 10^{-7} cm^{-1}. The method is elegantly simple in design and shows considerable promise because the apparatus would almost certainly be sufficiently robust for atmospheric field measurements.

The caveats alluded to above present obstacles to the measurement of absolute absorber amounts using this one-dimensional measurement of time-integrated intensity versus wavelength. Germane to the present discussion, Fielder et al. noted that their technique was affected by fluctuations in the intensity of the light source. It was particularly important that the lamp preserved its spectral intensity distribution for the duration of the measurements, although the authors proposed a twin-beam instrument in which the spectral distribution of the lamp can be monitored and used to correct for such variations. Moreover, like cavity-enhanced absorption with narrow-band lasers,[72] IBBCEAS provides absolute absorption measurements only if the reflectivity of the cavity's mirrors is known as a function of wavelength across the bandwidth of the measurement. The mirror reflectivity is either measured directly via conventional CRDS (for example, Fielder et al. used a scanned monochromatic source) or deduced from a IBBCEAS calibration spectrum of a known amount of an absorber with known cross section. Consequently, in its present demonstration, IBBCEAS is not a "stand alone" technique.

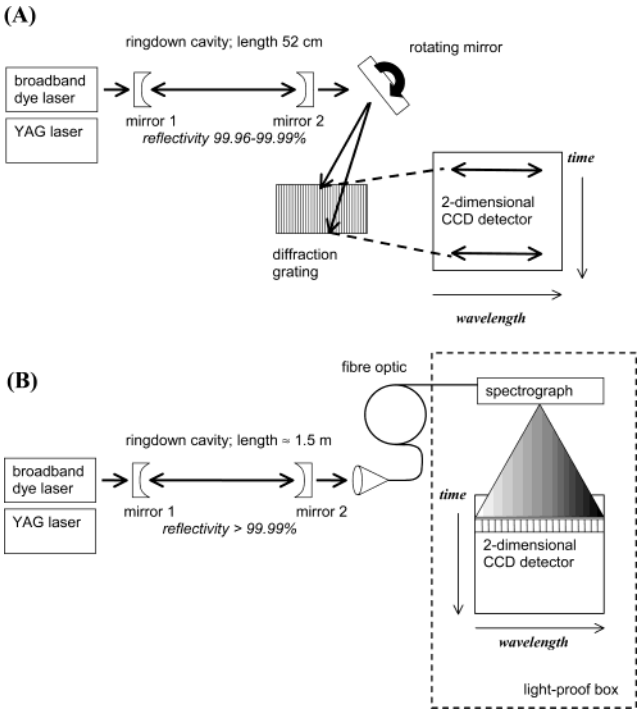

Figure 3. Schematic diagrams of (A) ring-down spectral photography (RSP) and (B) broad-band cavity ring-down spectroscopy (BBCRDS).

5.2. Two-Dimensional Broad-Band Cavity Ringdown Techniques

5.2.1. Ringdown Spectral Photography

In 1998, Scherer devised a technique he termed ring-down spectral photography (RSP)[101] in which radiation from a ring-down cavity was dispersed in time and wavelength and then imaged onto a two-dimensional detector array. The RSP apparatus is shown in Figure 3a. Radiation leaking from the ring-down cavity first encountered a mirror rotating at up to 6000 revolutions per minute. A sensor on the mirror mount's drive spindle was used to monitor the rotational period and to provide a trigger for the laser system. Upon reflection from the rotating mirror, the radiation was projected onto a diffraction grating such that its physical position on the grating was related to a time delay with respect to the laser pulse. The radiation was then dispersed according to its wavelength by the diffraction grating. The net result was the spatial dispersion of radiation along mutually perpendicular axes according first to the time it left the cavity and second its wavelength. Finally, the spatially dispersed cavity output was imaged onto a CCD camera. Thus, RSP achieved simultaneous time and wavelength resolution of the cavity output and consequently is a two-dimensional technique.

Ringdown spectral photography was demonstrated initially in a proof-of-principle study on propane.[101] The study used a sequence of discrete wavelengths

generated by tuning a conventional narrow-band dye laser in steps of 1 nm to mimic a broad-band source. At each step, the (monochromatic) cavity output was imaged to form a "streak" on the CCD where the position of the streak along the perpendicular axis of the CCD depended on the wavelength of the laser radiation. The spatially displaced decay steak images recorded in this way, one for each wavelength of the laser, were merged together to reveal the full spectral photograph at a resolution of 1 nm (see Figure 5 of ref 101).

Following refinement of the RSP instrument, a further study[102] in 2001 used broad-band radiation (0.13−0.5 mJ per pulse) from a YAG-pumped dye laser to record complete spectral photographs in a single laser shot. The ring-down cavity ($d = 52$ cm) consisted of two mirrors with reflectivities of approximately 99.99% near 630 nm and 99.96% near 690 nm. Impressive spectral photographs were produced of the 5th overtone of a C−H stretch in propane (which appears as a broad absorption band due to state congestion) and the rotationally resolved $b\ ^1\Sigma_g^+\ (v' = 1) \leftarrow X\ ^3\Sigma_g^-\ (v'' = 0)$ electronic transition in molecular oxygen. The spectral photograph of propane spanned the range 626−640 nm, while that of oxygen covered wavelengths 686−695 nm. The images were recorded on a subset of 640 × 480 pixels of a larger uncooled CCD, each pixel being 8 μm × 9 μm in size. The combination of the pixel size and the dispersion of the diffraction grating allowed spectral photographs to be acquired with a resolution up to 1.5 cm^{-1}. Thus, individual rotational lines are clearly visible in the spectral photograph of the oxygen sample (see Figure 5 of ref 102).

Scherer et al. also demonstrated that it was possible to extract quantitative absorption spectra from spectral photographs by fitting an exponential decay to the light intensity recorded in narrow slices of the image taken along the wavelength axis. An absorption spectrum of the propane sample was constructed in this way using slices from every 20th pixel and showed excellent agreement with an absorption spectrum of the same sample recorded by conventional step-scanned CRDS using a narrow-band dye laser. The uncertainty in the measured absorption deduced from the slice of the RSP image at 636 nm was estimated to be 2×10^{-8} cm^{-1}. This value is comparable with the sensitivity achievable by narrow-band CRDS in a single shot. However, importantly RSP produced a vast saving in acquisition time, having acquired the whole spectrum during a single pulse of the broad-band laser. The next step in the analysis would have been to demonstrate explicitly the quantitative nature of RSP by, for example, deducing the concentration of propane in the sample from a spectral fit of the absorption spectrum. Presumably the only reason Scherer et al. did not do so was because the wavelength-resolved cross sections were unavailable. Retrieval of the absorber amount from the spectral photograph of oxygen (for which the spectroscopy is known with great certainty) would have been more difficult—more on this topic in section 6.

In the present instrument, rotation of the mirror through just a few degrees of an arc was sufficient to disperse the cavity output across the full frame of the CCD. Although the stability of the mirror's motion was measured to be better than 15 ns per degree within a single revolution, the mechanism's driving motor possessed a long-term stability insufficient to permit light from successive ring-down events to be overlaid on the detector. Consequently, RSP by this method remains, to date, a single-shot technique. Scherer et al. noted that it is desirable to average a number of ring-down events to reduce fluctuations in the in the RSP images, particularly for those observed in the oxygen studies. It is possible that this could be done postacquisition by an analysis routine that realigns and then combines multiple images, though such a process would be time-consuming. Furthermore, the rate-limiting step in the acquisition of the spectral photograph from each laser shot is the process of reading the images from the CCD. Whereas the ring-down event is complete within a few hundred microseconds, the time taken to download an image from a CCD camera is of the order of one second. Though it can also be run in single-shot mode, the next related technique, developed independently, includes the capability to overlay and thus average directly the contributions from many ring-down events on the two-dimensional detector. The technique therefore acquires ring-down events with much greater frequency leading to an improved sensitivity within a given integration time.

5.2.2. Broad-Band Cavity Ringdown Spectroscopy

In 2001, we reported[82] studies on the NO_3 radical by broad-band cavity ring-down spectroscopy (BBCRDS) in which the cavity output was resolved in both time and wavelength simultaneously and imaged on a *clocked* two-dimensional charge-coupled device (CCD) detector. A schematic of the BBCRDS instrument is shown in Figure 3b. The absorption spectra of molecular oxygen, NO_3, and mixtures of NO_3 and water vapor presented to aid the discussion in later sections of this review were obtained with a refined version of this instrument with significantly improved sensitivity compared to our original work.

Pulsed broad-band radiation (∼5 mJ) was generated from a longitudinally pumped dye and Nd:YAG laser system operating at 20 Hz. The tuning grating had been removed from the dye laser cavity,[35] and in this way laser radiation covering a continuous range of >30 nm was generated dependent on the gain curve of the dye. The cavity consisted of two identical plano-concave mirrors separated by about 150 cm depending on the application. Two mirror pairs were used, both having their peak reflectivity close to 670 nm: approximately 99.995% the older pair used for the NO_3 studies and 99.999% for those of the oxygen studies. In both cases, the mirror reflectivity was found to vary smoothly with wavelength, a result that, where it occurs, can be used to advantage in the differential analysis of the ring-down spectra (section 6.3). Light exiting the ring-down cavity was collected and conveyed via an optical fiber to an astigmatic imaging spectrograph, and the

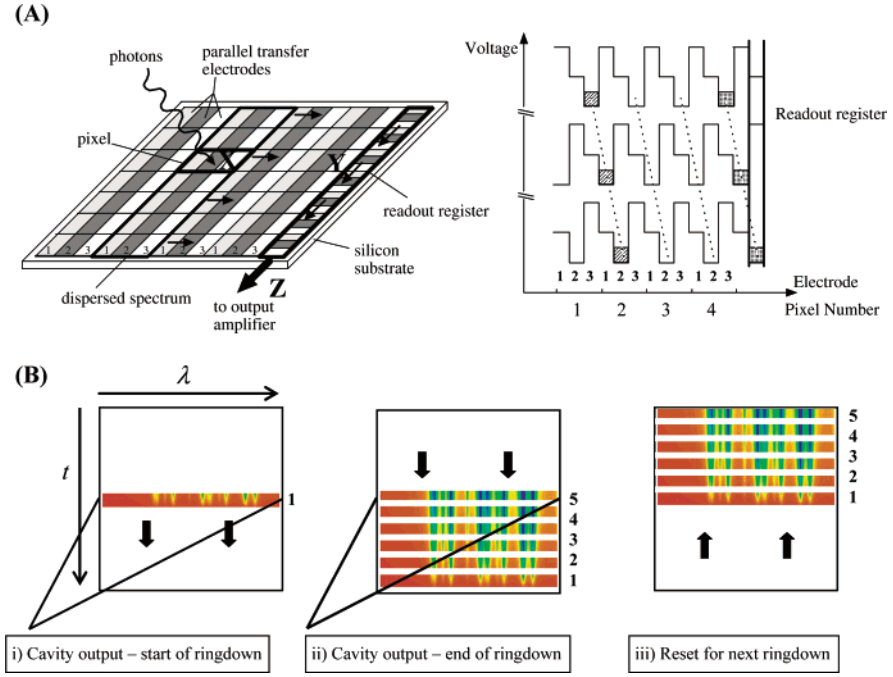

Figure 4. Schematic diagram of the principles of CCD operation. (A) Incident light is converted into photocharge (X) and stored in potential wells on the silicon layer. Three sets ofparallel transfer electrodes (shown as 1, 2, and 3 in both parts of A) are then charged cyclically to maintain a potential gradient across the device and push charge from pixel to pixel (X→Y). Finally, when photocharge from the first pixel has traversed the whole device, the charge is read out from the readout register to the output amplifier (Z). The voltage clocking sequence is shown on the right. (B) This illustrates how multiple spectra can be integrated on the CCD. (i) Photons from the cavity output are dispersed by the spectrograph and converted into photocharges on pixels in the unmasked part of the CCD. (ii) Time- and wavelength-resolved spectra are built up as photocharges are transferred downward by the clocking sequence. (iii) Once the complete ring-down event is recorded, charge is reverse clocked (upward in this case) to bring the first spectrum back to its original position to await a further capture sequence.

output image of the spectrograph was projected onto a clocked CCD perpendicular to the fast transfer axis. The laser was pulsed on a delayed trigger so that the clocking sequence initiated before radiation entered the cavity. The spectral resolution of the instrument was determined primarily by the choice of spectrograph grating and entrance slit width and was 0.1 and 0.2 nm fwhm in the O_2 and NO_3 studies, respectively. An imaging spectrometer, which uses torroidal mirrors to correct the spherical aberration inherent in the Czerny−Turner optical arrangement, was required so that the spectrum was not dispersed along the time axis, as this would have degraded the time resolution achievable.

Figure 4 illustrates the operation of the unique component of this instrument: the clocked CCD. A detailed account of CCD technology is given by Dereniak and Crowe.[103] The CCD chip itself was a 512 × 1024 array of 15 μm square pixels divided into image and storage areas of 512 × 512 each. Photocharge generated by the incident radiation and constrained by potential wells within each pixel was transferred efficiently (>99.9999%) between rows of CCD pixels in either direction by applying suitably phased voltages to the electrodes along one of the axes of the pixel array. The timing and sequence of these phased voltages along the time axis of the CCD are referred to as a clocking sequence (Figure 4A). Thus, the time-resolved spectra obtained in one transit of the chip were returned to their starting positions after the ring-down trace measurement to await the next laser pulse (Figure 4B). A mask was also used to prevent illumination of the unexposed parts of the CCD and to improve the definition of the 10 rows of pixels exposed to the incident radiation. With a maximum clocking rate of 0.5 μs per row, the instrument had a time resolution of 5 μs. Readout of charge from the CCD introduced a small source of noise; however, the electronics of the detection system were configured to allow the on-chip integration of ring-down events due to ≤255 laser pulses prior to readout, thus significantly increasing the ratio of signal to readout noise. The on-chip integration of many ring-down events gave the present system a further significant advantage over the single-shot RSP apparatus[101,102] because BBCRDS spectra are produced wherein shot-to-shot variations due to cavity mode beating have been averaged out.

Representative spectra obtained with this instrument are presented in sections 6 and 7 as illustrations both of the capabilities of cavity ring-down techniques using broad-band radiation and of some of the pit falls involved in the analysis of such spectra to yield absorber amounts. The quantitative retrieval of absorber amounts is, of course, a necessary requirement for the use of broad-band instruments in atmospheric observations but, as far as we are aware, has only been reported in the literature for NO_3 in laboratory samples.[82] Compared to NO_3, the narrow and optically thick absorption lines of atmospheric oxygen and water vapor present particular challenges to the spectral analysis. In sections 6.2 and 6.3 we present an easily implemented retrieval method based on a linear fit to the changing absorption cross

sections presented by molecular absorbers as the intracavity radiation travels increasing large path lengths back and forth between the cavity mirrors. This fitting procedure is demonstrated for spectra of the b ← X transition in molecular oxygen and applied in section 7.2 to the fitting of the water vapor structure that overlaps the 662 nm absorption band used to quantify atmospheric NO_3. The conclusions reached in these discussions are equally relevant to the analysis of spectra from other broad-band versions of the cavity ring-down technique.

6. b ← X Bands of Molecular Oxygen—A Test Case for Broad-Band Studies

The first (narrow-band) cavity ring-down spectrum reported by O'Keefe and Deacon, the originators of the technique, was of the b $^1\Sigma_g^+$ ($v' = 1,2$) ← X $^3\Sigma_g^-$ ($v'' = 0$) transitions of molecular oxygen.[49] Since then, several researchers have also chosen to use the fundamental (760 nm) and overtones (690 or 630 nm) of oxygen's atmospheric bands to demonstrate their particular advances in the field of cavity ring-down spectroscopy:

(1) Phase shift cavity ring-down spectroscopy[98]—Engeln et al., 1996;

(2) Fourier transform cavity ring-down spectroscopy[96]—Engeln & Meijer, 1996;

(3) Cavity-enhanced absorption and cavity-enhanced magnetic rotation spectroscopy[72]—Engeln et al., 1998;

(4) Integrated cavity output analysis[104]—O'Keefe, 1998;

(5) Pulsed single-mode cavity ring-down spectroscopy[63]—van Zee et al., 1999;

(6) Broad-band ring-down spectral photography[102]—Scherer et al., 2001;

(7) Fourier transform phase shift cavity ring-down spectroscopy[97]—Hamers et al., 2002;

(8) Incoherent broad-band cavity-enhanced absorption spectroscopy[100]—Fiedler et al., 2003.

Other groups have also applied CRDS to investigate the spectroscopy of these transitions for the oxygen isotopomers[105] or employed the bands in order to test or optimize their apparatus.[7,106,107] The spectroscopic line parameters[17] for these transitions are known accurately and, though weak in terms of conventional absorption spectroscopy, the line strengths are such that ring-down spectra can be obtained with excellent signal-to-noise ratios using only relatively modest cavity mirrors. However, the fine structure of the bands (line widths ≈ 0.1 cm^{-1} fwhm) cannot be fully resolved by any of the broad-band instruments reviewed in section 5. Additionally, these absorptions are optically thick at the very long optical path lengths accessible in cavity ring-down methods leading to non-Beer−Lambert law behavior, the correct treatment of which provides an exacting test of any analysis procedure that seeks to retrieve quantitative absorber amounts from broad-band cavity ring-down spectra. These complications are discussed further in section 6.1 et seq which uses the analysis of a broad-band spectrum of oxygen as an example to illustrate the quantitative nature of broad-band CRDS techniques even under spectroscopically unfavorable conditions.

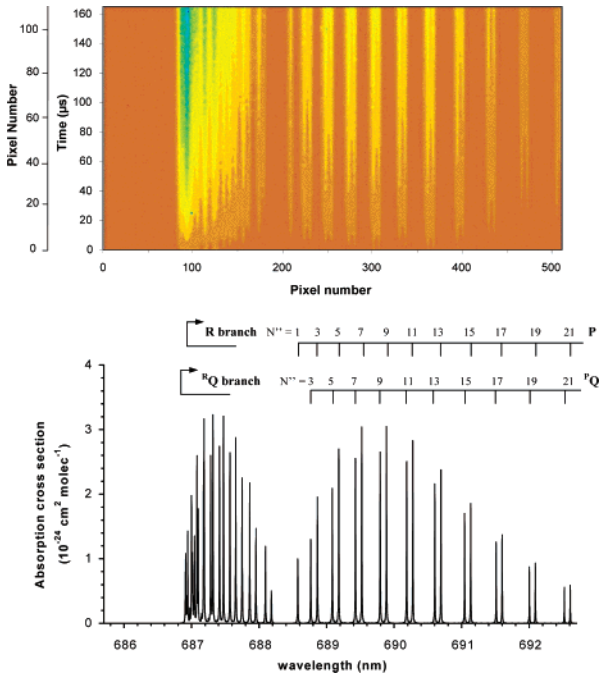

Figure 5. Cavity ring-down spectroscopy in two dimensions—A sample of 10% oxygen in nitrogen. The upper panel contains a plot of the wavelength- and time-dependent optical density, $OD(i,j)$, measured by each pixel (see text). The optical density corresponds with color as follows: red/orange, $OD(i,j) = 0$, yellow = 1, green = 2, blue = 3. The horizontal and outer vertical scales give the (i,j) pixel coordinates along the wavelength-dispersed and clocked axes of the CCD detector, respectively. The inner vertical axis gives the time delay for the clocking speed of 1.5 μs per pixel row. The lower panel shows the absorption cross sections of molecular oxygen from a line-by-line calculation using line parameters from the HITRAN database[17] (wavelengths are in a vacuum). The assignment of the rotational structure in the P and ^{P}Q branches is also shown.

Figure 5 shows an example of results obtained using our CCD detection system to monitor output from the cavity simultaneously as a function of wavelength and delay time. The upper panel of Figure 5 shows a contour map of the optical depth for a laboratory sample of 10% O_2 diluted in N_2 at 760 Torr. Note that the time dependence of the optical depth is a result of the time-dependent path length as light travels back and forth within the cavity, rather than any change in the absorber concentration. The optical depth was calculated from the natural logarithm of the ratio of the counts registered by each pixel for spectra recorded first by flowing the O_2/N_2 mixture through the cavity (sample) and then flushing the cavity with pure N_2 (flush), following the subtraction in both cases of any dark count signal

$$OD(i,j) = \ln\frac{\text{counts}_{\text{flush}}(i,j)}{\text{counts}_{\text{sample}}(i,j)} \qquad (7)$$

The horizontal scale and the outer vertical scale of the color plot give the (i,j) coordinates of the ith pixel along the wavelength dispersed axis of the CCD

for the *j*th step of the clocking sequence. The clocking speed was 1.5 μs per pixel row, and the inner scale of the vertical *j*-axis gives the time delay after the laser pulse (160 μs corresponds to an optical path length of 48 km). Taking the ratio as in eq 7 removes contributions to the measured optical depth from losses that are common to both the sample and the flushed cavities, i.e., mirror absorption and transmission losses, and molecular Rayleigh scattering at one atmosphere pressure (Rayleigh scattering by O_2 and N_2 is assumed to be the same: a difference would in any case result only in a smoothly varying continuum absorbance that would be removed by the DOAS analysis that follows). Figure 5 was composed using data averaged from 10 sample and 10 flush spectra, each spectrum being the on-chip integration of 255 ring-down events. The total acquisition time for the batch of 10 sample spectra (2550 ring-down events) was approximately 150 s including the time taken to read the images from the CCD. The batch of 10 flush spectra took another 150 s to acquire, though for a sequence of measurements it would usually be necessary to acquire flush spectra only periodically to check for degradation in the reflectivity of the cavity mirrors.

The wavelength calibration for the data in Figure 5 was provided by comparison of the differential structure of the measurement with oxygen absorption cross sections obtained from a line-by-line calculation at the appropriate temperature and partial pressures of O_2 and N_2. The lower panel of Figure 5 shows the absorption cross sections calculated at high resolution using line parameters given in the HITRAN spectral database.[17] Compared to the measurement shown in the contour plot above, the calculated cross sections exhibit clearer differential structure because they are not limited by the resolution of the present instrument.

To confirm the quantitative nature of broad-band CRDS techniques, it is necessary to compare the concentration of O_2 deduced from spectral fitting of the measurement shown in Figure 5 with the known O_2 amount in the sample. However, before fitting the data, we review the processes that lead to non-Beer–Lambert law behavior and hence multiexponential decays in broad-band cavity ring-down measurements that are unable to fully resolve the spectral transitions. We use the data shown in Figure 5 as our example.

6.1. Multiexponential Ringdown Decays in Broad-Band CRDS

As noted in section 4, a significant complication arises in the analysis of cavity ring-down spectra if the spectral width of the probe radiation is comparable to or exceeds the widths of the molecular absorption features.[60] The analogous issue for broad-band studies is whether the spectral resolution of the detection system is sufficient to fully resolve the molecular absorption features. We have already stated that the spectral resolution (≈0.1 nm fwhm) of the instrument that acquired the data in Figure 5 is more than an order of magnitude larger than the width of the oxygen absorption lines (≈0.1 cm^{-1} fwhm, equivalent to 0.005 nm at 690 nm). A similar comment applies to the other broad-band instruments reviewed above (Table 1).

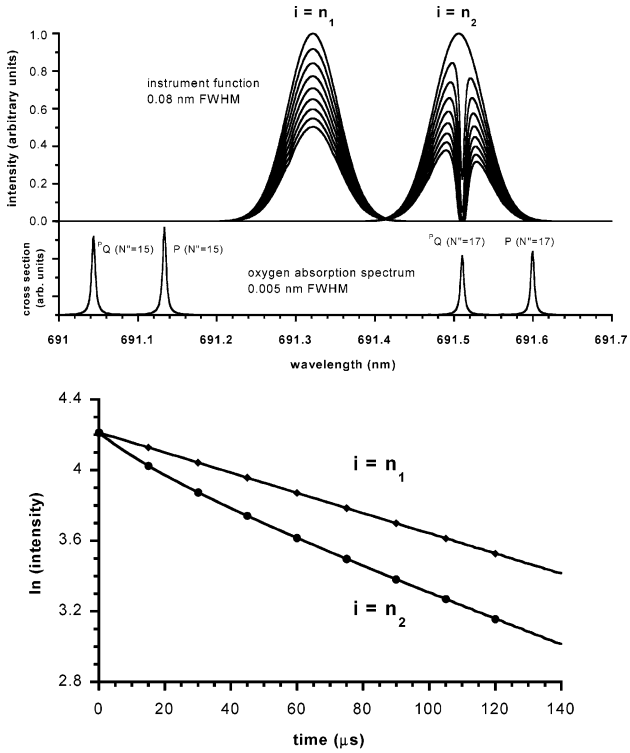

Figure 6. Origin of multiexponential ring-down decays—A simulation for 10% oxygen at atmospheric pressure. The upper panel shows the range of wavelengths incident on pixels n_1 and n_2 due to the instrument resolution (represented by a Gaussian of 0.08 nm fwhm and unit amplitude centered at 691.32 and 691.51 nm). The cavity output sampled onto these pixels is shown at intervals of 15 μs, assuming that oxygen is the only structured absorber within the sample and that the ring-down time of the cavity is 180 μs without absorption by O_2. Here, the instrument function is more than an order of magnitude wider than the oxygen absorption lines. The lower panel shows the natural logarithm of the total signal recorded by pixels n_1 and n_2 as a function of time, calculated from the area under the curves of decaying amplitude in the upper panel.

Figure 6 illustrates how the limited spectral resolution of a broad-band instrument leads to multiexponential ring-down decays, in this case in a simulation for sample of oxygen. (Note that the same effect arises in conventional narrow-band CRDS where the molecular absorption lines are narrower than the line width of the laser.) The simulation treats the instrument function as a Gaussian of 0.08 nm fwhm, shown in the upper panel of Figure 6 as the two broad features of unit amplitude for pixels $i = n_1$ and n_2. (In the pixel coordinates of Figure 5, $n_1 = 414$ corresponds to $\lambda = 691.32$ nm and $n_2 = 428$ corresponds to $\lambda = 691.51$ nm). The first of these pixels records cavity output where there is no $^{16}O_2$ structure, although there are very weak features due to the less abundant O_2 isotopomers. However, the second pixel receives cavity output attenuated by the $N'' = 17$ line of the ^PQ branch of $^{16}O_2$. The nested curves of decreasing amplitude show the calculated time evolution of the spectral energy incident on these pixels at intervals of 15 μs. The calculation assumed that the only structured absorption was that

by 10% O_2 in N_2 at atmospheric pressure and used a ring-down time of 180 μs to account for the combination of mirror losses and Rayleigh scattering.

The signal recorded by each pixel column during ring-down decay corresponds to the integrated area under the nested curves shown in the upper panel of Figure 6. The natural logarithm of this signal is plotted as a function of time in the lower panel. For $i = n_1$, this appears as a straight line because all wavelength components within the envelope of the instrument function decay at a single rate determined in this simulation entirely by the reflectivity of the cavity mirrors and Rayleigh scattering. This is the familiar case of a ring-down decay that is a simple exponential function, and a fit to these data returns the ring-down time of 180 μs previously assumed in the calculation. For pixel column $i = n_2$, however, cavity output on-resonance with the O_2 absorption feature decays far more rapidly than radiation at other wavelengths also sampled by this pixel column. Hence, the ring-down signal cannot be adequately described by a single-exponential function and the logarithm of signal versus time shows pronounced curvature.

As noted at the beginning of section 5, narrow-band CRDS measurements have been made successfully under conditions where the spectral width of the probe radiation exceeds that of the molecular absorption features by ensuring that the absorption by the sample was small.[60,95] A convenient way to arrange this was to consider only those data acquired for relatively few passes of the cavity (i.e., at short times, $t \ll \tau$). This was equivalent to deducing a ring-down time from the gradient of the decaying signal at the short time limit. However, such an option is undesirable for broad-band ring-down measurements in the atmosphere because it would severely compromise the sensitivity of a measurement that relies on the very long path lengths accessible by the CRDS technique. Therefore, the analysis of broad-band ring-down spectra requires the presence of multiexponential ring-down decays to be considered explicitly. In the current analysis this is achieved through the use of an effective or *linearized* absorption spectrum.

6.2. Linearization of Absorption in Broad-Band CRDS Spectra

One approach to the analysis of broad-band CRDS spectra could be to fit the two-dimensional (time, wavelength) absorption measurement to calculations using a suitable nonlinear multivariable least-squares approach into which a high-resolution line-by-line transmission code has been embedded. In other words, a simulation akin to that in section 6.1 could be run iteratively for the oxygen concentration until the rate, and especially the curvature, in the simulated decays matched the experimental data for all wavelength bins of the CCD detector. However, an equivalent and computationally much less costly approach, and the one suggested here, is to use an effective or *linearized* absorption cross section for the molecular absorber at the resolution of the instrument that accounts accurately for the apparent change in absorption cross section during the ring-down period due to saturation of the absorption process at line center. Linearized cross sections are produced in the following manner.

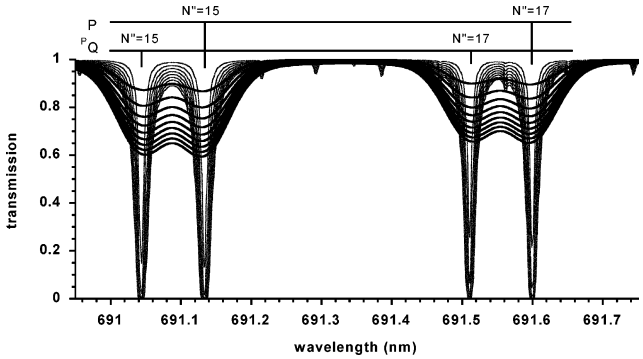

Figure 7. Transmission spectra calculated for column amounts of oxygen encountered by photons confined within the cavity for 15, 30, ..., 135 μs, equivalent to optical path lengths of 4.5, 9.0, ..., 40.5 km. The lighter gray lines are high-resolution transmission spectra calculated using the oxygen absorption cross sections from a line-by-line calculation. The thicker black lines are the corresponding transmission spectra at the resolution of the BBCRDS instrument obtained from a convolution of the high-resolution transmission spectra with the measured instrument function (see text).

Step 1: Column amounts of the absorber, $u(t)$, encountered by the intracavity radiation as it is reflected back and forth within the cavity are calculated for an initial trial value for the absorber concentration, x_0, for times t spanning the range of the ring-down signal

$$u(t) = x_0 ct \tag{8}$$

where c is the speed of light. High-resolution absorption cross sections produced from a line-by-line calculation, $\sigma(\lambda)$, are then used to calculate the transmission spectrum for each column amount of the absorber

$$trans(\lambda,t) = \exp[-\sigma(\lambda)u(t)] \tag{9}$$

The lighter traces in Figure 7 show examples of high-resolution transmission spectra in the portion of the oxygen spectrum between 690.95 and 691.75 nm, calculated in intervals of 15 μs for times $t = 15-135$ μs for a sample of 10% O_2 at atmospheric pressure. The region includes the $N'' = 15$ and 17 lines of both the P and ^{P}Q branches of $^{16}O_2$ (the other weak transitions are due to the less abundant isotopomers). It is clear from Figure 7 that the radiation at the line centers is highly attenuated: the transmission at line center is approximately 0.2 even for the earliest spectrum at $t = 15$ μs.

Step 2: The high-resolution transmission spectra at each time step are independently convolved with the instrument function to yield time-dependent transmission spectra degraded to the resolution of the instrument, $trans_{inst}(\lambda,t)$. This latter set of spectra is shown as the solid black curves in Figure 7.

Step 3: The procedure now is to produce linearized absorption cross sections from the variation of $trans_{inst}(\lambda,t)$ with $u(t)$ at the center wavelength appropriate for each pixel column of the detector. The

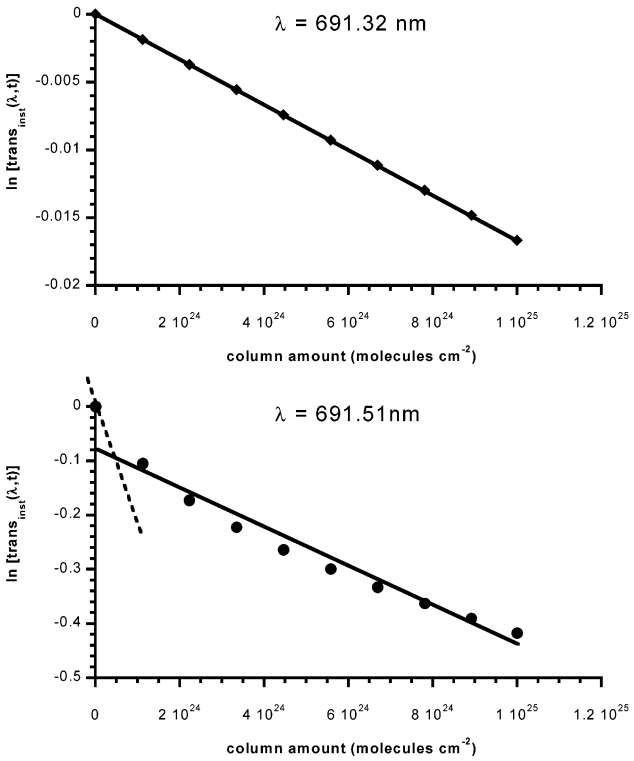

Figure 8. Transmission of the 10% oxygen sample at the resolution of the BBCRDS instrument versus the column amount of the absorber encountered by radiation trapped in the cavity for 15, 30, ..., 135 μs. The upper and lower panels are for wavelengths off- and on-resonance with a strong absorption line, respectively, and the solid points are taken directly from the transmission spectra of Figure 7 at the appropriate wavelengths. At $\lambda = 691.32$ nm, where absorption by oxygen is weak, the linear relationship indicates that the absorption can be described by a constant cross section. However, the data for $\lambda = 691.51$ nm exhibit pronounced curvature attributable to substantial changes in spectral shape around strong absorption lines that become saturated at the long optical paths of the BBCRDS measurement. Linear fits are shown for comparison, and these are used below to calculate the linearized absorption cross sections, $\sigma^*(\lambda)$ (see text). The gradient of the dashed line in the lower panel indicates the absorption cross section for a short path length.

gradient of a linear fit to the variation of the natural logarithm of $trans_{inst}(\lambda,t)$ with $u(t)$ is thus a linear approximation to the (changing) absorption cross section at wavelength λ. For consistency with the later discussion, this quantity is termed the linearized molecular absorption cross section $\sigma^*(\lambda)$, where the asterisk indicates that the linearization process has been performed.

Figure 8 shows explicitly the linearization of cross sections at two test wavelengths, $\lambda = 691.32$ and 691.51 nm, off- and on-resonance with oxygen absorption lines. The solid points are the natural logarithm of $trans_{inst}(\lambda,t)$ at times $t = 0-135$ μs, the data having been taken directly from Figure 7 at the relevant time steps and wavelengths. The solid diamonds ($\lambda = 691.32$ nm) fall on a straight line, the gradient of which is the (negative of the) linearized absorption cross section, $\sigma^*(\lambda)$. The sample is optically thin at this wavelength in the far wings of the oxygen lines, and the linearized absorption cross section is essentially the same as that which would be obtained

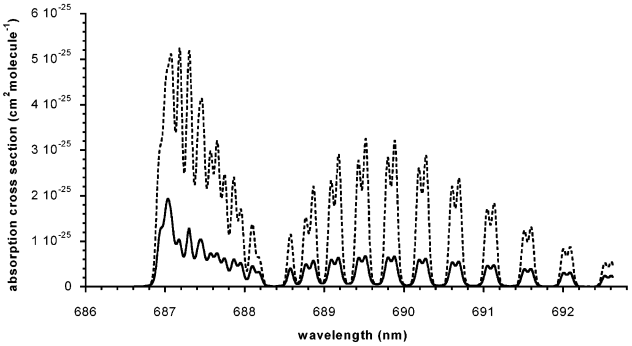

Figure 9. Oxygen absorption cross sections calculated at the resolution of the BBCRDS instrument for the full wavelength range of the present measurements. The dotted line shows the cross sections appropriate for absorption over a short path length, and these were obtained by convolving the high-resolution cross sections directly with instrument function. The heavy black line shows the linearized absorption cross sections that parametrize the absorption over the very long path lengths travelled by radiation while confined within the ring-down cavity.

if the high-resolution absorption cross sections $\sigma(\lambda)$ had been convolved directly with the instrument function. However, crucially for $\lambda = 691.51$ nm, the solid circles do not fall on a straight line, indicating that the shape of the absorption spectrum around this wavelength changes during the ring-down event—the linearized absorption cross section now represents an average of the changing cross section encountered by the radiation while reflected back and forth within the ring-down cavity. Note that $\sigma^*(\lambda)$ at this wavelength is substantially different from the absorption cross section at the limit of high dilution (represented by the gradient of the dashed line) obtained by convolving the high-resolution absorption cross section directly with the instrument function.

The heavy black line in Figure 9 shows linearized absorption cross sections calculated by the above method for wavelengths spanning the (1,0) band of O_2. For comparison, the dotted line represents the oxygen absorption cross sections appropriate for an optically thin sample, obtained by convolving the high-resolution cross sections directly with the instrument function. The two spectra in Figure 9 show marked differences both in the magnitude of the absorption cross section and in the shape of the spectrum. As anticipated above, the regions of strong absorption appear less pronounced in the linearized spectrum (most noticeable near the band head at 687 nm).

The justification for adopting the above approach is presented in Figure 10, where the results of a calculation of $trans_{inst}(\lambda,t)$ are compared with the experimentally determined O_2 optical depths shown previously in Figure 5. The open points are the negative of the measured optical depths versus time for pixel columns corresponding to n_1 (diamonds; $\lambda = 691.32$ nm) and n_2 (circles; $\lambda = 691.51$ nm). Because the measured optical depths have been derived from the ratio of pixel counts in the sample and flush files (eq 7), the contributions from mirror losses and Rayleigh scattering have already been removed, leaving only attenuation by oxygen within the sample. Thus, the measured optical depths can be compared

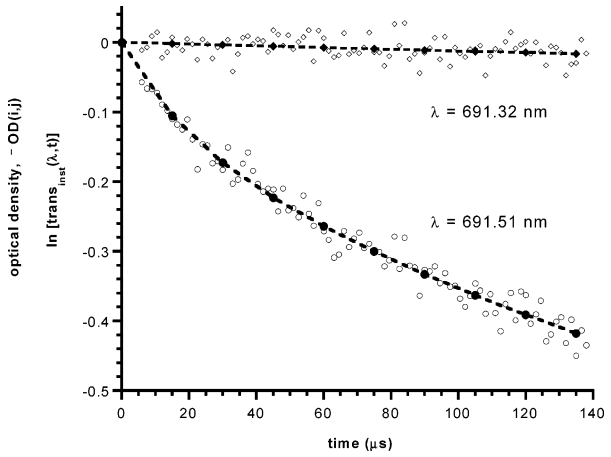

Figure 10. Comparison of the calculated column-dependent transmission with the BBCRDS measurements on the sample of 10% oxygen. The comparison is shown for wavelengths off- and on-resonance with a strong absorption line. The open points are the negative of the optical depth, $-OD(i,j)$, taken at the appropriate wavelengths from the color plot in the upper panel of Figure 5. The solid points are the transmission data shown previously in Figure 8, though here shown as a function of the time that the photons were confined in the ring-down cavity.

directly with the calculated transmission data (solid points) to show that the curvature observed in the multiexponential ring-down decays even on resonance with saturated absorption lines can be reproduced by the above spectral calculations. Thus, the linearized absorption cross sections accurately describe the path-length-averaged cross sections presented by the sample over the range of wavelengths within the envelope of the instrument function for the various column amounts encountered by the radiation while trapped in the cavity. In turn, this confirms that a spectrum of measured *linearized ring-down times*, where the ring-down decay is approximated using a single-exponential function with a 1/e decay time of $\tau^*(\lambda)$ regardless of whether the decay at that wavelength is in fact multiexponential, can indeed be reproduced theoretically. The linear fits of ln(*signal*) versus *t* in the broad-band ring-down data that produce $\tau^*(\lambda)$ and the linear fits in the spectral calculation that produce $\sigma^*(\lambda)$ must be conducted over the same range in delay times and corresponding column amounts, respectively.

The problem of recovering the O_2 concentration from the data now resembles a DOAS analysis where a linearized cross section $\sigma_i^*(\lambda)$ of species *i* is fitted to an absorbance spectrum $\alpha^*(\lambda)$ calculated using measured linearized ring-down times from the sample spectra $\tau^*(\lambda)$. Equation 10 is the analogue of eq 6 adapted for this calculation using the aforementioned quantities designated with an asterisk

$$\frac{1}{\tau^*(\lambda)} = \frac{1}{\tau(\lambda)} + c\alpha^*(\lambda) = \frac{1}{\tau(\lambda)} + c\sum_i \sigma_i^*(\lambda)\, x_i \qquad (10)$$

The spectral calculation requires the O_2 absorber amount to be known, and in practice, an iterative procedure using a trial first guess is employed.

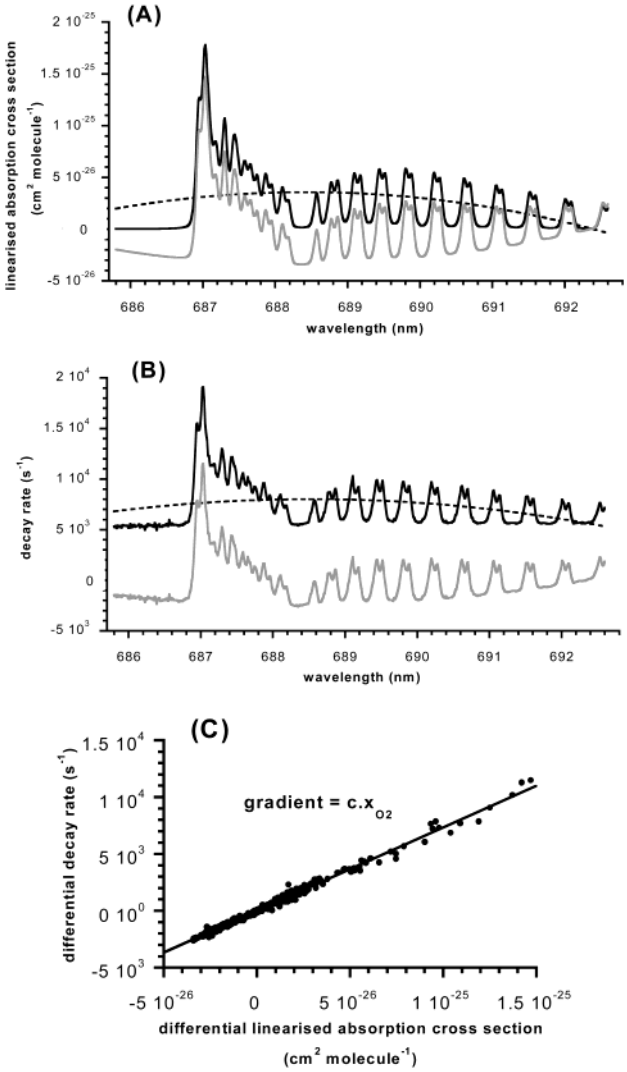

Figure 11. Differential fitting of the measured BBCRDS absorption spectrum of a sample of 10% oxygen at standard atmospheric pressure. (A) The linearized absorption cross section, $\sigma^*(\lambda)$, is shown as the solid black line which is fitted with a quadratic function (dashed line). Subtraction of the quadratic yields the differential linearized absorption cross sections, $\Delta\sigma^*(\lambda)$ (gray line). (B) The measured decay rate, $k^*(\lambda)$, of the wavelength-dependent ring-down signal (solid black line). Subtraction of a quadratic fit to these data (the dashed line) yields the differential decay rate, $\Delta k^*(\lambda)$ (gray line). (C) A linear fit to a plot of the differential quantities generated in parts A and B, where the gradient of the line gives the oxygen concentration multiplied by the speed of light.

6.3. Quantitative retrieval of Absorber Amounts Using Linearized Absorption Cross Sections

Except for the use of linearized absorption cross sections calculated according to the method outlined above, the differential fitting of absorbances measured via single-exponential fits to broad-band ring-down decays follows the standard DOAS procedure introduced in section 3. First, a polynomial of order *n* is fitted to the linearized absorption cross sections, for example, see part A of Figure 11 where $n = 2$. The fitted polynomial is then subtracted from the linearized cross sections to yield a differential linearized absorption cross section, $\Delta\sigma^*(\lambda)$, represented by the gray curve. The procedure of polynomial fitting

and subsequent subtraction would normally be repeated on the measured absorbances calculated from eq 10 to yield a differential absorption spectrum, $\Delta\alpha^*(\lambda)$. However, owing to the very long path lengths accessed in with the present instrument, small residuals due to oxygen absorption were observed in the data for the flush spectra, implying incomplete flushing of the ring-down cavity. Consequently, in this example, differential fits were performed on the rate of decay of the ring-down signal averaged over the batch of 10 sample data alone, where the decay rate is defined as $k^*(\lambda) = 1/\tau^*(\lambda)$, and as before the asterisk denotes the linear fit. Note that the mirror losses and Rayleigh scattering cause the decay rates to be offset from zero even at wavelengths where oxygen does not absorb (part B of Figure 11). Fitting and subtraction of the polynomial yielded a differential decay rate $\Delta k^*(\lambda)$ in the usual way. The choice of fitting either $\Delta k^*(\lambda)$ or $\Delta\alpha^*(\lambda)$ has no effect on the retrieval of the absorber amount from the wavelength-dependent differential structure via the DOAS analysis provided that the slowly varying contribution to the decay rate due to the mirror losses and Rayleigh scattering can be fitted accurately by the polynomial used to generate $\Delta k^*(\lambda)$.

The remaining analysis was straightforward for this sample, which was known to contain just a single structured absorber. Part C of Figure 11 shows a plot of $\Delta k^*(\lambda)$ versus $\Delta\sigma^*(\lambda)$ together with a linear fit to the data, the gradient of which gives the absorber concentration multiplied by the speed of light. That there is a close linear relationship between $\Delta k^*(\lambda)$ and $\Delta\sigma^*(\lambda)$ at all wavelengths provides further validation of use linearized absorption cross sections to parametrize the absorption process during the ring-down event. The fitted O_2 mixing ratio of (9.85 $\pm$ 0.04)% is in good agreement with the expectation of a 10% mixture, and the difference from the expected value is comfortably within the combined uncertainties in the calibrations of the O_2 and N_2 flow controllers. The uncertainty in the mixing ratio quoted here is the 1σ statistical uncertainty, i.e., the standard deviation in the gradient of the linear fit of $\Delta k^*(\lambda)$ versus $\Delta\sigma^*(\lambda)$.

An excellent agreement between the fitted O_2 spectrum and the measured BBCRDS spectrum is shown in the comparison in Figure 12. The lower line offset to negative values of the absorbance is the residual spectrum, i.e., the measured spectrum minus the fitted oxygen spectrum. The standard deviation (rms) in the residual spectrum is 6.25×10^{-9} cm^{-1} and is comparable to the baseline noise in conventional CRDS spectroscopy. Examination of the DOAS literature shows that least-squares fits to individual atmospheric spectra can produce unreasonably small statistical errors that underestimate the true uncertainty of the measurement. In many respects, the standard deviation of the residual spectrum is a better estimate of the uncertainty in the broad-band ring-down measurement than the statistical (random) error deduced from the spectral fitting routine. This is because the former includes contributions from systematic errors including unknown or ill-defined absorption and scattering by other components not considered in the spectral fitting routine

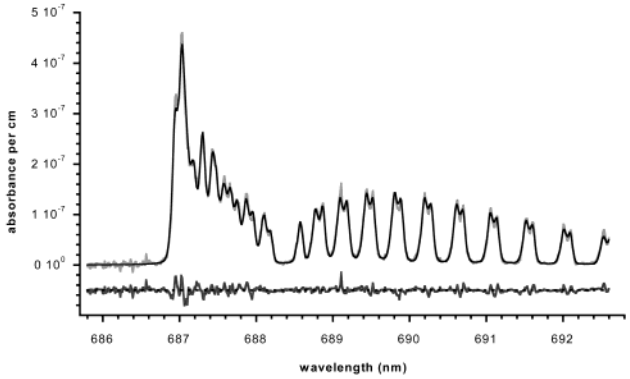

Figure 12. Fitted BBCRDS spectrum for the 10% sample of oxygen. The measurement is shown as the lighter gray line, here the decay rate divided by the speed of light, $k^*(\lambda)/c$. In addition, a quadratic function accounting for the mirrors losses and Rayleigh scattering has been subtracted from the measurement (i.e., the smoothly varying baseline underlying the differential structure of part B of Figure 11 has been removed). The solid black line overlaid on the measurements is the fitted oxygen spectrum (mixing ratio of 9.85 $\pm$ 0.04%). The residual spectrum offset to negative values is the measured spectrum minus the fitted spectrum and has a standard deviation of 6.25×10^{-9} cm^{-1}.

or the failure to fit molecular absorption cross sections that properly account for absorption processes. By way of an example, a second data set was acquired for a 20% mixture of O_2 diluted with N_2 at standard atmospheric pressure. The analysis of these data began (deliberately and erroneously) using the linearized cross sections for the 10% mixture and returned a mixing ratio of (14.77 $\pm$ 0.08)%, well below the known dilution. The origin of the error is obvious: the curvature in the measured ring-down decays on-resonance with the oxygen absorption lines was greater than could be accounted for by the linearized absorption cross sections appropriate for the 10% mixture. Moreover, the statistical error returned by this analysis was unreasonably small owing to the large systematic error introduced by fitting incorrect cross sections. Fortunately, the analysis is robust and can be iterated to yield an accurate measurement of an (unknown) absorber amount by recalculating linearized absorption cross sections for successive absorbers amount returned by the spectral fitting procedure. On iteration, the fitted amount for the sample of oxygen diluted to 20% tended to a figure of (19.70 $\pm$ 0.08)%, in agreement within the 1σ statistical uncertainty with the figure of (19.80 $\pm$ 0.08)% resulting from a single iteration that used linearized cross sections calculated for a 20% mixing ratio. Both figures agreed with the known dilution within the systematic uncertainty due to the calibration of the O_2 and N_2 flow controllers.

In summary, quantitative absorber amounts have been retrieved from broad-band spectra of molecular oxygen, which, owing to the narrowness and optical thickness of the absorption features, resulted in pronounced curvature in the wavelength-resolved, multiexponential ring-down signals. The pressure broadened widths of the rotationally resolved absorption lines of water vapor[17,26] ($\approx$0.2 cm^{-1} fwhm or 0.01 nm at 650 nm) are also narrower than the resolution of all current broad-band instruments. Thus, the

above procedure demonstrated on oxygen is also applicable to quantification and spectral stripping of water vapor from atmospheric broad-band ring-down spectra to permit fitting of the overlapping spectrum of broad-band absorbers such as NO_3. The following section considers the quantitative measurement of NO_3 by broad-band cavity ring-down spectroscopy on laboratory samples of NO_3 and NO_3/water mixtures.

7. Measurement of the NO_3 Radical by Broad-Band Methods

As discussed above, Brown et al.[74−76,93] and Simpson[69] already demonstrated narrow-band CRDS instruments with sufficient sensitivity to detect ambient levels of NO_3 and N_2O_5. Respectively, the instruments had detection limits of 0.25 pptv for both NO_3 and N_2O_5 (1σ uncertainty in a 5 s integration) and 2.4 pptv for N_2O_5 and 1.7 pptv for NO_3 (both 2σ limits for a 25s integration). The sensitivity of the Brown et al. instrument in particular compares favorably with the sensitivity of the well-established DOAS instruments, typically 1 pptv for NO_3.[36,39,45] Additionally, Ball et al.[82] demonstrated a broad-band cavity ring-down instrument able to measure NO_3 in laboratory samples with a sensitivity of 2 pptv (12 min integration). To aid discussion on the quantitative retrieval of absorber amounts in atmospheric applications, we now show examples of broad-band spectra of NO_3 acquired with the refined version of our BBCRDS instrument. These spectra also show an improved sensitivity in a reduced acquisition time compared to our previous work. Finally, we show broad-band spectra of laboratory samples of a mixture containing NO_3 and water vapor to demonstrate how quantitative amounts of both absorbers can be retrieved for a simultaneous DOAS-type fitting process through the use of linearized absorption cross sections.

7.1. Broad-Band Spectra of NO_3

In common with long-path DOAS field instruments, the CRDS instruments referred to in the previous paragraph monitor NO_3 via its broad absorption band around 662 nm due to the B $^2E' \leftarrow$ X $^2A'_2$ electronic transition. The spectral width this absorption band is approximately 3.5 nm fwhm[18,22−24] and therefore is more than an order of magnitude wider than the resolution of the authors' BBCRDS instrument. Indeed, the other broad-band instruments listed in Table 1 would also be able to record the spectrum of a similarly broad absorber in laboratory samples without the issue of the saturation of strong, narrow absorption lines arising.

The upper panel of Figure 13 shows a contour map of the optical density for a sample of NO_3 in nitrogen carrier gas measured simultaneously as a function of both wavelength and delay time during the ring-down event. As for the oxygen sample (Figure 5), the time dependence of the optical depth is due to the increasing path length of the measurement as the intracavity light undergoes multiple reflections. In these experiments, NO_3 was produced in situ within the ring-down cavity from the thermal decomposition

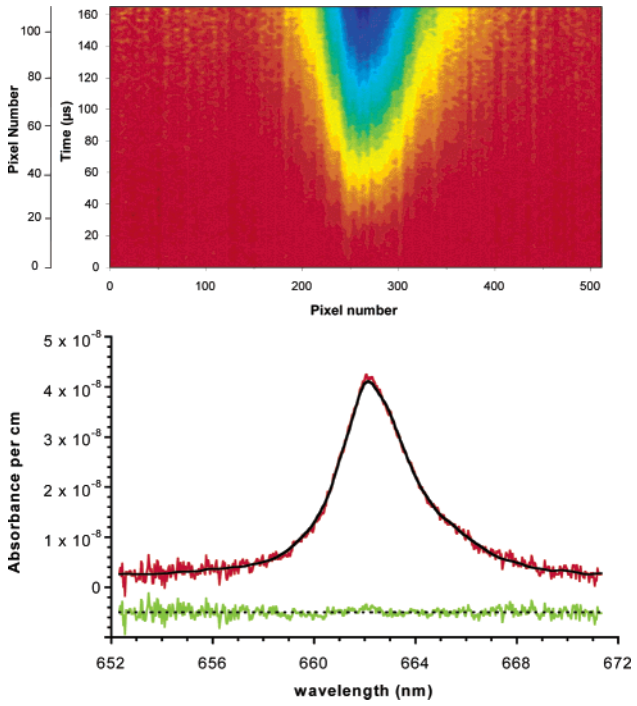

Figure 13. Cavity ring-down spectroscopy in two dimensions—NO_3. The upper panel contains a plot of the wavelength- and time-dependent optical density, $OD(i,j)$, measured by each pixel (see text). The optical density corresponds with color as follows: red, $OD(i,j) = 0$, orange/yellow = 0.05, light green = 0.1, sky blue = 0.15, blue = 0.2. The CCD was clocked at 1.5 μs per pixel row. The lower panel shows the measured BBCRDS absorbance spectrum, $\alpha(\lambda)$, as the red line. The black line is the absorption due to NO_3 (94.37 ± 0.47 pptv) and NO_2 (6 ± 2 ppbv) plus a small baseline and was obtained from fitting molecular absorption cross sections to the measured spectrum in differential space (quadratic fits). The residual spectrum (green line) is the difference between the measured and fitted spectra and has a standard deviation of 1.18×10^{-9} cm^{-1}.

of N_2O_5 entrained into the gas flow upstream of the cavity by passing a portion of the flow over a sample of N_2O_5 held a 196 K. The data in Figure 13 were calculated using eq 7 from the average of 10 spectra for both the sample and the nitrogen flush, each spectrum being the on-chip integration of 200 laser shots, i.e., for the sample, a total of 2000 laser shots acquired in 130 s.

For this spectrally broad absorber, the wavelength-resolved absorbance, $\alpha(\lambda)$, was calculated using eq 6, fitting simple exponential decays with time constants of $\tau'(\lambda)$ and $\tau(\lambda)$, respectively. $\alpha(\lambda)$ was then fitted by a quadratic function which on subtraction yielded the differential absorbance, $\Delta\alpha(\lambda)$. The differential NO_3 absorption cross sections, $\Delta\sigma_{NO3}(\lambda)$, were calculated by applying a quadratic fit directly to the data of Yokelson et al.[23] at 298 K, after first shifting the cross sections to longer wavelengths by a small amount (0.27 nm). In the present case, calibration of the wavelength scale came from a comparison of the differential water structure in the NO_3/H_2O spectra (see following section) with linearized absorption cross sections generated from the ESA spectral database[26] which lists its line frequencies in a vacuum (the Yokelson et al. data are air wavelengths). However, very recently, Orphal et al.[24] remeasured the NO_3 spectrum, and preliminary

results indicate that marginally smaller residuals were obtained when fitting the present NO_3 spectra with the new cross sections (listed in a vacuum, so no wavelength shift was necessary). This implies that the new cross sections are better able to reproduce both the position and shape of the NO_3 band.

NO_2 was also produced inside the ring-down cavity from the thermal decomposition of the N_2O_5 precursor. It was further likely that excess NO_2 was present in the sample due to the heterogeneous conversion of N_2O_5 and NO_3 to NO_2 on the walls of the cavity and associated tubing and that the N_2O_5 sample itself contained NO_2 impurities. Although the NO_2 cross section[21] at 662 nm is more than 3 orders of magnitude smaller than that of NO_3, absorption by NO_2 became significant at wavelengths in the tail of the NO_3 band if the concentration of NO_2 exceeded that of NO_3 by more than about an order of magnitude. Therefore, the amount of NO_3 in the sample was retrieved from a simultaneous fit of $\Delta\alpha(\lambda)$ for $\Delta\sigma_{NO3}(\lambda)$, $\Delta\sigma_{NO2}(\lambda)$ and a quadratic baseline to account for other unknown absorption terms such as degradation of the mirror reflectivity—more on the fitting of spectra for multiple species in the next section. The uncertainty in the NO_3 concentration quoted for the BBCRDS spectra is the 1σ standard deviation in the fit of $\Delta\sigma_{NO3}(\lambda)$ to $\Delta\alpha(\lambda)$ and so does not include the uncertainty in the absolute value of the NO_3 cross sections (10% at 662 nm[23]).

The lower panel in Figure 13 shows the measured BBCRDS spectrum (red) corresponding to the data in the color map plot above. The absorber amounts retrieved by the fitting procedure were NO_3 (94.3 ± 0.5 pptv) and NO_2 (6 ± 2 ppb), and the NO_3 figure represents a significant improvement in sensitivity since our previous work.[82] The black line overlaid on the BBCRDS spectrum is the calculated absorption spectrum due to the fitted NO_3 and NO_2 amounts plus the fitted (quadratic) baseline. The residual spectrum offset to negative values of the absorbance (green line) is the difference between the measured and fitted spectra. The standard deviation of the residual spectrum is 1.18×10^{-9} cm^{-1}. The data in Figure 14 show further examples of BBCRDS spectra and their fitted composite spectra for samples containing smaller amounts of NO_3. Note that the statistical uncertainty in the fitted NO_3 amount is under 0.5 pptv in both panels of Figure 14. The noise in the residual spectra is usually greatest at the wavelength extremes of the spectra where the lower gain of the laser dye leads to greater photon (shot) noise—most evident when absorption by the sample is small. This suggests that the measurement precision could be increased further if a truly broad-band light source were available. The lower panel of Figure 14 illustrates another advantage of acquiring data simultaneously across a broad spectral range. The signal-to-noise ratio near the peak of the NO_3 absorption band is less than unity, yet the NO_3 absorption is clear from a visual inspection of the figure. Moreover, the fitted NO_3 absorbance is statistically significant because it is derived from a large number of measurements across the absorption band rather than two observations at wavelengths on- and off-resonance.

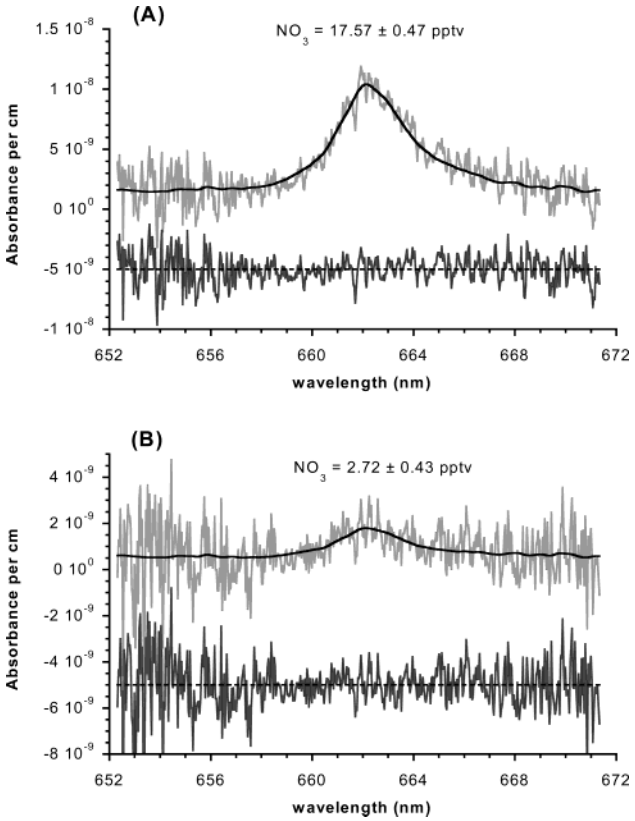

Figure 14. Further examples of BBCRDS spectra and fits for NO_3 samples. (A) $NO_3 = 17.57 \pm 0.47$ pptv; $NO_2 = 4.2 \pm 1.7$ ppbv; standard deviation of residual spectrum = 1.17×10^{-9} cm^{-1}. (B) $NO_3 = 2.72 \pm 0.43$ pptv; $NO_2 = 1.7 \pm 1.6$ ppbv; standard deviation of residual spectrum = 1.07×10^{-9} cm^{-1}.

7.2. Simultaneous Analysis of Multiple Species from Broad-Band Spectra: NO_3 and Water Vapor

As indicated in section 3, a particularly desirable feature of the DOAS methodology is that, because of the inherent spectral oversampling, it can be applied successfully to situations where the absorption spectra of a number of species overlap. A necessary condition is that the cross sections of the absorbing species possess sufficiently distinguishable structure or have absorptions that vary so smoothly with wavelength that the high-pass filtering process removes them completely. The measurement of atmospheric NO_3 using it 662 nm absorption band is one such case where quantification of the target species is compromised by overlapping structure due to other absorbers, here overtone bands of H_2O within the $4\nu+\delta$ polyad centered at 652 nm[17,26,108]. Part A of Figure 15 shows the absorption cross sections of both the broad NO_3 spectrum[23] and the much sharper vibration−rotation spectrum of H_2O, the latter from a line-by-line calculation using line parameters from the ESA database.[26] Traditionally, DOAS measurements of NO_3 have required the simultaneous fitting of absorption features of both species including the effects of non Beer−Lambert law behavior for the stronger H_2O transitions which become saturated under atmospheric conditions.[48]

Part B of Figure 15 shows an example of a BBCRDS spectrum of a mixed NO_3 and H_2O sample obtained by present instrument under laboratory

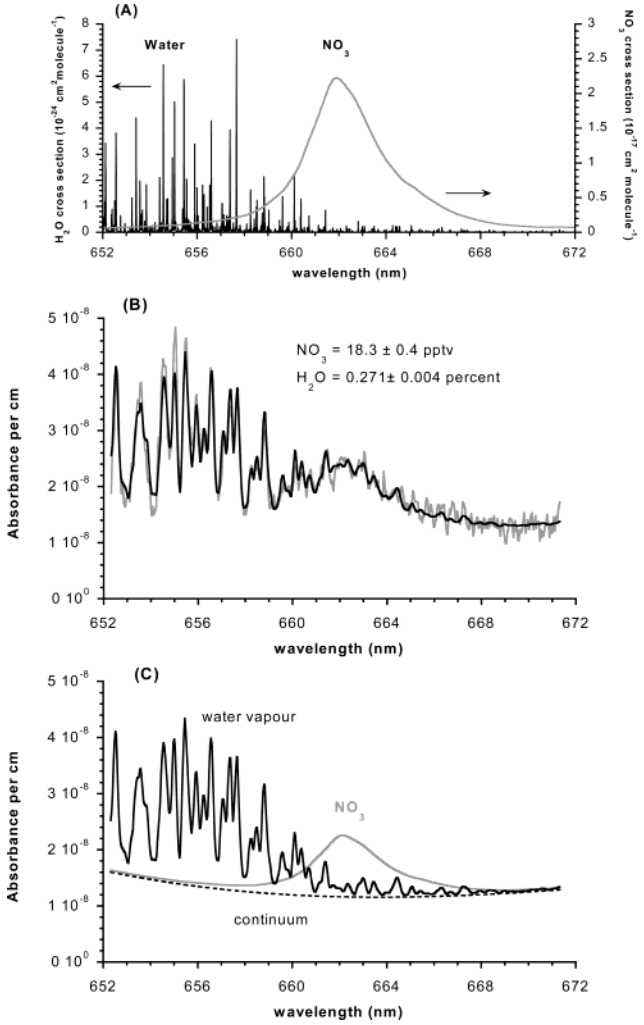

Figure 15. BBCRDS spectra of a sample containing water vapor and NO_3. (A) NO_3 absorption cross sections of Yokelson et al.[23] at 298 K and the water vapor absorption cross sections from a line-by-line calculation using parameters from the ESA spectral database.[26] (B) Linearized absorbance, $\alpha^*(\lambda)$, from BBCRDS measurements on a laboratory sample containing both NO_3 and water vapor (gray line). The black line overlying the measurement is the fitted spectrum resulting from a simultaneous differential fit ($n = 2$) of the NO_3 cross section, the water vapor cross section at the resolution of the instrument linearized by the method described in the text, and a quadratic function to describe a substantial continuum absorption (probably due to water aerosol generated in the humidifier). (C) Components of the fitted spectrum: a continuum absorption (dashed line) and added to it absorption spectra due to NO_3 (gray line) or water vapor (black line).

conditions (grey line). Because the water vapor absorption lines were narrower than the instrument resolution, the linearized approach was used to calculate the sample absorbance, $\alpha^*(\lambda)$, via eq 10 from values of $\tau^*(\lambda)$ obtained from the average of 10 sample acquisitions and values of $\tau(\lambda)$ from 10 flushed acquisitions. Note the significant absorption offset apparent in the spectrum even at long wavelengths where absorption by neither NO_3 nor the H_2O monomer is strong. Here the continuum absorption is thought to be due to extinction by water aerosol generated in the humidifier, although the effects of broad H_2O dimer absorption may also be present.[109]

In addition, part B of Figure 15 shows the composite fitted spectrum (black line) resulting from a simultaneous fit of three quantities to the differential absorption spectrum: (1) the differential NO_3 cross section, (2) the differential linearized H_2O cross section calculated by the method introduced in section 6.2, and (3) a quadratic function to account for the continuum absorption. As before, quadratic functions were applied to the spectra and cross sections to generate the differential quantities. The mixing ratios fitted by this procedure are 18.3 ± 0.4 pptv for NO_3 and $(0.271 \pm 0.004)\%$ for H_2O. Again, the NO_3 amount has been retrieved with sub-pptv uncertainty, though here in the presence of an overlapping absorption feature. The fitted composite spectrum is decomposed into its constituent parts in part C of Figure 15, as the absorption spectra of water vapor (solid line) or of NO_3 (gray line) added to the fitted continuum (dotted line).

8. Summary

In this paper we reviewed briefly the fundamentals of "traditional" cavity ring-down spectroscopy (CRDS) using essentially monochromatic light sources and the use of such techniques in quantifying weak absorptions. The relatively few CRDS experiments in the literature that have used broad-band radiation sources were reviewed in greater detail because of their ability to collect information about a sample's absorption over a range of wavelengths during a single ring-down event. This aspect of broad-band instruments offers substantial potential for the measurements of important trace species in the atmosphere as has been demonstrated with the now well-established DOAS technique reviewed at the beginning of the paper. The marriage of DOAS and CRDS methodologies in broad-band cavity ring-down instruments has been shown in this review to provide a route to in situ point measurements with selectivities and sensitivities comparable to the DOAS approach. Consequently, such instruments have applications in the attribution of local sources/sinks and the investigation of small-scale chemical processing in the atmosphere.

The apparatus and analysis procedures required for broad-band instruments were described in some detail because the widths of certain target (or interfering) molecules' absorption lines are narrower than the resolution of any broad-band instrument constructed to date. We took as our example molecular oxygen whose absorption lines are particularly narrow compared to the instrumental resolution, leading to pronounced multiexponential character in the ring-down signals which must be properly quantified if broad-band techniques are to lead to quantitative measurements of narrow-band absorbers. A retrieval method was introduced based on the fitting of differential spectral structure through the use of linearized absorption cross sections to account for non Beer−Lambert character of intermediate or strong absorptions. This approach obviates many of the difficulties faced previously in the analysis of broad-band cavity ring-down spectra.

Examples of broad-band cavity ring-down measurements on laboratory samples containing NO_3 and both NO_3 and H_2O were also presented. These examples demonstrated that, since information is gathered across the entire absorption band of, in this case NO_3, attribution of the differential structure in the resulting spectrum via DOAS methods leads to sub-pptv accuracy for NO_3 mixing ratios even in the presence of overlapping absorptions. The analysis has the additional advantage that any continuum absorption may be determined directly from the measured spectrum, providing important ancillary measurement of the aerosol optical depth for atmospheric studies.

In their current configurations and with the continuing development of new radiation sources, broad-band cavity ring-down techniques are proving to be an extremely exciting development of DOAS, which complements the traditional long-path DOAS approach in terms of selectivity and sensitivity. However, in contrast, the intrinsic length of CRDS measurements is the length of the ring-down cavity (typically less than one meter), hence broad-band cavity ring-down instruments extend measurements to small spatial scales which are proving to be of increasing scientific interest.

While we focused almost exclusively on the visible and near UV regions of the spectrum, we note that DOAS/broad-band CRDS can be extended to other wavelengths. In principle, the broad-band techniques reviewed here could be extended into the near-infrared, where many important atmospheric species have absorption features (although complete coverage of the infrared will require an advance in detector technology because the quantum efficiency of current CCDs falls rapidly at long wavelengths). While retaining the ability to survey large spectral regions rapidly, the advantages of the DOAS approach are less obvious in the near-IR, where molecular absorptions are typically the narrow lines of ro-vibrational transitions and where absorption and scattering by aerosol particles is less efficient.[1,76] At such wavelengths, narrow-band instruments based on, for example, CW external cavity diode lasers may prove to be the CRDS technique of choice for measuring atmospheric absorbers with resolved rotational spectra. However, there is a class of vitally important atmospheric species, the peroxy radicals,[4] HO_2, CH_3O_2, $C_2H_5O_2$, etc., which have electronic transitions around 1.3 μm. The absorption spectrum of HO_2 is congested but is rotationally resolved,[110] whereas the larger radicals exhibit broad absorption bands.[10,111,112] The detection of these species by cavity ring-down spectroscopy has already been demonstrated in the laboratory[10,112] and proposed as a method for measuring these species in the atmosphere.[10] Their broad absorption bands seemingly make them prime candidates for future broad-band cavity ring-down studies.

9. Acknowledgments

Our initial broad-band cavity ring-down spectroscopy study on NO_3 was supported by a "small research grant" (GR9/04411) from United Kingdom's Natural Environment Research Council (NERC). Dr. Ball holds a NERC Advanced Research Fellowship.

10. References

(1) Finlayson-Pitts, B. J.; Pitts, J. N., Jr. *Chemistry of the Upper and Lower Atmosphere*; Academic Press: San Diego, CA, 1999.
(2) Brasseur, G. P.; Orlando, J. J.; Tyndall, G. S. *Atmospheric Chemistry and Global Change*; Oxford University Press: New York, 1999.
(3) Wayne, R. P. *Chemistry of Atmospheres*, 3rd ed.; Oxford University Press: Oxford, 2000.
(4) Atkinson, R. *Atmos. Environ.* **2000**, *34*, 2063.
(5) Parrish, D. D.; Fehsenfeld, F. C. *Atmos. Environ.* **2000**, *34*, 1921.
(6) Scherer, J. J.; Paul, J. B.; O'Keefe, A.; Saykally, R. J. *Chem. Rev.* **1997**, *97*, 25.
(7) Wheeler, M. D.; Newman, S. M.; Orr-Ewing, A. J.; Ashfold, N. M. R. *J. Chem. Soc., Faraday Trans.* **1998**, *94*, 337.
(8) *Cavity ring-down spectroscopy: an ultratrace-absorption measurement technique*; Busch, K. W., Busch, M. A., Eds.; American Chemical Society: Washington, DC, 1999.
(9) Berden, G.; Peeters, R.; Meijer G. *Int. Rev. Phys. Chem.* **2000**, *19*, 565.
(10) Atkinson, D. B. *Analyst* **2003**, *128*, 117.
(11) Brown, S. S. *Chem. Rev.* **2003,** *103*, 5219.
(12) Platt, U. Differential Optical Absorption Spectroscopy (DOAS). In *Air Monitoring by Spectroscopic Techniques*; Sigrist, M. W., Ed.; Chemical Analysis Series; John Wiley: New York, 1994; Vol. 127, p 27.
(13) Plane, J. M. C.; Smith, N. Atmospheric monitoring by Differential Optical Absorption Spectroscopy. In *Spectroscopy in Environmental Science, Advances in Spectroscopy*; Clark, R. J. H., Hester, R. E., Eds.; John Wiley & Sons Ltd.; Chichester, U.K., 1995; Vol. 24, p 223.
(14) Platt, U. *Phys. Chem. Chem. Phys.* **1999**, *1*, 5409.
(15) Stephens, G. L. *Remote Sensing in the Lower Atmosphere: An Introduction*; Oxford University Press: Oxford, 1994.
(16) Clark, R. J. H.; Hester, R. E. *Spectroscopy in Environmental Science, Advances in Spectroscopy*; John Wiley & Sons Ltd.: Chichester, U.K., 1995; Vol. 24.
(17) Rothman, L. S.; Rinsland, C. P.; Goldman, A.; Massie, S. T.; Edwards, D. P.; Flaud, J. M.; Perrin, A.; Camy-Peyret, C.; Dana, V.; Mandin, J.-Y.; Schroeder, J.; McCann, A.; Gamache, R. R.; Wattson, R. B.; Yoshino, K.; Chance, K. V.; Jucks, K. W.; Brown, L. R.; Nemtchinov, V.; Varanasi, P. *J. Quant. Spectrosc. Rad. Transfer* **1998**, *60*, 665.
(18) DeMore, W. B.; Sander, S. P.; Golden, D. M.; Hampson, R. F.; Kurylo, M. J.; Howard, C. J.; Ravishankara, A. R.; Kolb, C. E.; Molina, M. J. *Chemical Kinetics and Photochemical Data for Use in Stratospheric Modeling, Evaluation Number 12*, JPL publication 97-4, Jet Propulsion Laboratory: Pasadena, CA, 1997.
(19) Brion, J.; Chakir, A.; Charbonnier, J.; Daumont, D., Parisse, C.; Malicet, J. *J. Atmos. Chem.* **1998**, *30*, 291.
(20) Atkinson, R.; Baulch, D. L.; Cox, R. A.; Crowley, J. N.; Hampson, R. F., Jr; Kerr, J. A.; Rossi, M. J.; Troe, J. *J. Phys. Chem. Ref. Data* **2000**, *29*, 167.
(21) Vandaele, A. C.; Hermans, C.; Simon, P. C.; van Roozendael, M.; Guilmot, J. M.; Carleer, M.; Colin, R. *J. Atmos. Chem.* **1996**, *25*, 289.
(22) Wayne, R. P.; Barnes, I.; Biggs, P.; Burrows, J. P.; Canosa-Mas, C. E.; Hjorth, J.; Le Bras, G.; Moortgat, G. K.; Perner, D.; Poulet, G.; Restelli, G.; Sidebottom, H. *Atmos. Environ.* **1991**, *25A*, 203.
(23) Yokelson, R. J.; Burkholder, J. B.; Fox, R. W.; Talukdar, R. K.; Ravishankara, A. R. *J. Phys. Chem.* **1994**, *98*, 13144.
(24) Orphal, J.; Fellows, C. E.; Flaud, P.-M. *J. Geophys. Res.* **2003**, *108* (D3) 4077.
(25) Schermaul, R.; Learner, R. C. M.; Canas, A. A. D.; Brault, J. W.; Polyansky, O. L.; Belmiloud, D.; Zobov, N. F.; Tennyson, J. *J. Mol. Spectrosc.* **2002**, *211*, 169.
(26) Schermaul, R.; Zobov, N. F.; Learner, R. C. M.; Newnham, D. A.; Ballard, J.; Tennyson, J. *J. Mol. Spectrosc.*, submitted for publication. Files containing the spectroscopic line parameters can be downloaded from http://badc.nerc.ac.uk/data/esa-wv.
(27) Liu, X.; Murcray, F. J.; Murcray, D. G.; Russell, J. M. *J. Geophys. Res.* **1996**, *101*, 10175.
(28) Rodgers, C. D. *Inverse Methods for Atmsopheric Sounding: Theory and Practice*; World Scientific Publishing Co.: Singapore, 2000.
(29) Platt, U.; Perner, D. *J. Geophys. Res.* **1980**, *85*, 7453.
(30) Platt, U.; Perner, D.; Schroder, J.; Kessler, C.; Toennissen, A. *J. Geophys. Res.* **1981**, *86*, 1965.
(31) Platt, U.; Perner, D. Measurements of Atmospheric Trace Gases by Long Path Differential UV/Visible Absorption Spectroscopy. In *Optical and Laser Remote Sensing*; Killinger, D. A., Mooradien, A., Eds.; Springer-Verlag: New York, 1983; p 95.
(32) Hubler, G.; Perner, D.; Platt, U.; Toennisen, A.; Ehhalt, D. H. *J. Geophys. Res.* **1984**, *89*, 1309.

(33) Weaver, A. R.; Solomon, S.; Sanders, R. K.; Arapag, K.; Miller, H. L. *J. Geophys. Res.* **1996**, *94*, 11041.
(34) Aliwell, S. R.; Jones, R. L. *J. Geophys. Res.* **1998**, *103*, 5719.
(35) Povey, I. M.; South, A. M.; t'Kint de Roodenbeke, A.; Hill, C.; Freshwater R. A.; Jones, R. L. *J. Geophys. Res.* **1998**, *103*, 3369.
(36) Allan, B. J.; Carslaw, N.; Coe, H.; Burgess, R. A.; Plane, J. C. M. *J. Atmos. Chem.* **1999**, *33*, 129.
(37) Geyer, A.; Alicke, B.; Mihelcic, D.; Stutz, J.; Platt, U. *J. Geophys. Res.* **1999**, *104*, 26097.
(38) Wagner, T.; Otten, C.; Pfeilsticker, K.; Pundt, I.; Platt, U. *Geophys. Res. Lett.* **2000**, *27*, 3441.
(39) Geyer, A.; Alicke, B.; Konrad, S.; Schmitz, T.; Stutz, J.; Platt, U. *J. Geophys. Res.* **2001**, *106*, 8013.
(40) Hausmann, M.; Platt, U. *J. Geophys. Res.* **1992**, *99*, 25399.
(41) Alicke, B.; Hebestreit, K.; Stutz, J.; Platt, U. *Nature* **1999**, *397*, 572.
(42) Allan, B. J.; McFiggans, G.; Plane, J. M. C.; Coe, H. *J. Geophys. Res.* **2000**, *105*, 14363.
(43) Frieβ, U.; Wagner, T.; Pundt, I.; Pfeilsticker, K.; Platt, U. *Geophys. Res. Lett.* **2001**, *28*, 1941.
(44) Allan, B. J.; Plane, J. M. C.; McFiggans, G. *Geophys. Res. Lett.* **2001**, *28*, 1945.
(45) Plane, J. M. C.; Nien, C.-F. *Rev. Sci. Instrum.* **1991**, *63*, 1867.
(46) Armerding, W.; Comes, F. J.; Crawack, H. J.; Forberich, O.; Gold, G.; Ruger, C.; Spiekermann, M.; Walter, J.; Cuevas, E.; Redondas, A.; Schmitt, R.; Matuska, P. *J. Geophys. Res.* **1997**, *102*, 10603.
(47) Press: W. H.; Teukolsky, S. A.; Vetterling, W. T.; Flannery, B. P. *Numerical Recipies in C: the Art of Scientific Computing*, 2nd ed.; Cambridge University Press: Cambridge, 1992.
(48) Aliwell, S. R.; Jones, R. L. *Geophys. Res. Lett.* **1996**, *23*, 2585.
(49) O'Keefe, A.; Deacon, D. A. G. *Rev. Sci. Instrum.* **1988**, *59*, 2544.
(50) Hallock, A. J.; Berman, E. S. F.; Zare, R. N. *Anal. Chem.* **2002**, *74*, 1741.
(51) Xu, S.; Sha, G.; Xie, J. *Rev. Sci. Instrum.* **2002**, *73*, 255.
(52) Snyder, K. L.; Zare, R. N. *Anal. Chem.* **2003**, *75*, 3086.
(53) Engeln, R.; von Helden, G.; van Roij, A. J. A.; Meijer, G. *J. Chem. Phys.* **1999**, *110*, 2732.
(54) Kleine, D.; Lauterbach, J.; Kleinermanns, K., Hering, P. *Appl. Phys. B* **2001**, *72*, 249.
(55) Logunov, S.; *Appl. Opt.* **2001**, *40*, 1570.
(56) Marcus, G. A.; Schwettman, H. A. *Appl. Opt.* **2002**, *41*, 5167.
(57) Sappey, A. D.; Hill, E. S.; Settersten, T.; Linne, M. A. *Opt. Lett.* **1998**, *23*, 954.
(58) Thompson, J. E.; Smith, B. W.; Winefordner, J. D. *Anal. Chem.* **2002**, *74*, 1962.
(59) Vander Wal, R. L.; Ticich, T. M. *Appl. Opt.* **1999**, *38*, 1444.
(60) Zalicki, P.; Zare, R. N. *J. Chem. Phys.* **1995**, *102*, 2708.
(61) Hodges, J. T.; Looney J. P.; van Zee, R. D. *J. Chem. Phys.* **1996**, *105*, 10278.
(62) Meijer, G.; Boogaarts, M. G. H.; Jongma, R. T.; Parker D. H.; Wodtke, A. M. *Chem. Phys. Lett.* **1994**, *217*, 112.
(63) Van Zee, R. D.; Hodges, J. T.; Looney, J. P. *Appl. Opt.* **1999**, *38*, 3951.
(64) Romanini, D.; Kachanov, A. A.; Sadeghi, N.; Stoeckel, F. *Chem. Phys. Lett.* **1997**, *264*, 316.
(65) Romanini, D.; Kachanov, A. A.; Stoeckel, F. *Chem. Phys. Lett.* **1997**, *270*, 538.
(66) He, Y.; Hippler, M.; Quack, M. *Chem. Phys. Lett.* **1998**, *289*, 527.
(67) Schulz, K. J.; Simpson, W. R. *Chem. Phys. Lett.* **1998**, *297*, 523.
(68) Mazurenka, M. I.; Fawcett, B. L.; Elks, J. M. F.; Shallcross, D. E.; Orr-Ewing, A. J. *Chem. Phys. Lett.* **2003**, *367*, 1.
(69) Simpson, W. R. *Rev. Sci. Instrum.* **2003**, *74*, 3442.
(70) Paldus, B. A.; Harb, C. C.; Spence, T. G.; Wilke, B.; Xie, J.; Harris, J. S.; Zare, R. N. *J. Appl. Phys.* **1998**, *83*, 3991.
(71) Spence, T. G.; Harb, C. C.; Paldus, B. A.; Zare, R. N.; Willke B.; Byer, R. L. *Rev. Sci. Instrum.* **2000**, *71*, 347.
(72) Engeln, R.; Berden, G.; Peeters, R.; Meijer, G. *Rev. Sci. Instrum.* **1998**, *69*, 3763.
(73) O'Keefe, A.; Scherer, J. J.; Paul, J. B. *Chem. Phys. Lett.* **1999**, *307*, 343.
(74) Brown, S. S.; Stark, H.; Ciciora, S. J.; Raviskankara, A. R. *Geophys. Res. Lett.* **2001**, *28*, 3227.
(75) Brown, S. S.; Stark, H.; Ciciora, S. J.; McLaughlin, R. J.; Raviskankara, A. R. *Rev. Sci. Instrum.* **2002**, *73*, 3291.
(76) Brown, S. S.; Stark, H.; Raviskankara, A. R. *Appl. Phys. B* **2002**, *75*, 173.
(77) King, M. D.; Dick, E. M.; Simpson, W. R. *Atmos. Environ.* **2000**, *34*, 685.
(78) Vasudev, R.; Usachev, A.; Dunsford, W. R. *Environ. Sci. Technol.* **1999**, *33*, 1936.
(79) Czyzewski, A.; Chudzynski, S.; Ernst, K.; Karasinski, G.; Kilianek, L.; Pietruczuk, A.; Skubiszak, W.; Stacewicz, T.; Stelmaszczyk, K.; Kock, B.; Rairoux, P. *Opt. Commun.* **2001**, *191*, 271.
(80) Evertsen, R.; Staicu, A.; Dam, N.; van Vliet, A.; Ter Meulen, J. J. *Appl. Phys. B*, **2002**, *74*, 465.
(81) Lauterbach, J.; Kleine, D.; Kleinermanns, K.; Hering, P. *Appl. Phys. B* **2000**, *71*, 873.
(82) Ball, S. M.; Povey, I. M.; Norton, E. G.; Jones, R. L. *Chem. Phys. Lett.* **2001**, *342*, 113.
(83) Wang, L.; Zhang, J. *Environ. Sci. Technol.* **2000**, *34*, 4221.
(84) Naus, H.; Ubachs, W.; Levelt, P. F.; Polyansky, O. L.; Zobov, N. F.; Tennyson, J. *J. Mol. Spectrosc.* **2001**, *205*, 117.
(85) Jongma, R. T.; Boogaarts, M. G. H.; Holleman, I.; Meijer, G. *Rev. Sci. Instrum.* **1995**, *66*, 2821.
(86) Cheskis, S.; Derzy, I.; Lozovsky, V. A.; Kachanov, A.; Romanini, D. *Appl. Phys. B* **1998**, *66*, 377.
(87) Barry, H. R.; Bakowski, B.; Corner, L.; Freegarde, T.; Hawkins, O. T. W.; Hancock, G.; Jacobs, R. M. J.; Peveral, R.; Ritchie, G. A. D. *Chem. Phys. Lett.* **2000**, *319*, 125.
(88) Wheeler, M. D.; Newman, S. M.; Ishiwata, T.; Kawasaki, M.; Orr-Ewing, A. J. *Chem. Phys. Lett.* **1998**, *285*, 346.
(89) Ninomiya, Y.; Hashimoto, S.; Kawasaki, M.; Wallington, T. J. *Int. J. Chem. Kinet.* **2000**, *32*, 125.
(90) Newman, S. M.; Howie, W. H.; Lane, I. C.; Upson, M. R.; Orr-Ewing, A. J. *J. Chem. Soc., Faraday Trans.* **1998**, *94*, 2681.
(91) Atkinson, D. B.; Hudgens, J. W.; Orr-Ewing, A. J. *J. Phys. Chem. A*, **1999**, *103*, 6173.
(92) Ashworth, S. H.; Allan, B. J.; Plane, J. M. C. *Geophys. Res. Lett.* **2002**, *29* (10), 65
(93) Brown, S. S.; Stark, H.; Ryerson, T. B.; Williaims, E. J.; Nicks, D. K.; Trainer, M.; Fehsenfeld, F. C.; Ravishankara, A. R. *J. Geophys. Res.* **2003**, *108*, 4299.
(94) Romanini, D.; Lehmann, K. K. *J. Chem. Phys.* **1993**, *99*, 6287.
(95) Newman, S. M.; Lane, I. C.; Orr-Ewing, A. J.; Newnham, D. A.; Ballard, J. *J. Chem. Phys.* **1999**, *110*, 10749.
(96) Engeln, R.; Meijer, G. *Rev. Sci. Instrum.* **1996**, *67*, 2708.
(97) Hamers, E.; Schram, D.; Engeln, R. *Chem. Phys. Lett.* **2002**, *365*, 237.
(98) Engeln, R.; von Helden, G.; Berden, G.; Meijer, G. *Chem. Phys. Lett.* **1996**, *262*, 105.
(99) Crosson, E. R.; Haar, P.; Marcus, G. A.; Schwettman, H. A.; Paldus, B. A.; Spence, T. G.; Zare, R. N. *Rev. Sci. Instrum.* **1999**, *70*, 4.
(100) Fiedler, S. E.; Hese, A.; Ruth, A. A. *Chem. Phys. Lett.* **2003**, *371*, 284.
(101) Scherer, J. J. *Chem. Phys. Lett.* **1998**, *292*, 143.
(102) Scherer, J. J.; Paul, J. B.; Hong, J.; O'Keefe, A. *Appl. Opt.* **2001**, *40*, 6725.
(103) Dereniak, E. L.; Crowe. D. G. *Optical Radiation Detectors*; John Wiley: New York, 1984.
(104) O'Keefe, A. *Chem. Phys. Lett.* **1998**, *293*, 331.
(105) Naus, H.; van der Weil, S. J.; Urbachs, W. *J. Mol. Spectrosc.* **1998**, *192*, 162.
(106) Kim, J. W.,; Yoo, Y. S.; Lee, J. Y.; Lee, J. B.; Hahn, J. W. *Appl. Opt.* **2001**, *40*, 5509.
(107) Bakowski, B.; Corner, L.; Hancock, G.; Kotchie, R.; Peverall, R.; Ritchie, G. A. D. *Appl. Phys. B* **2002**, *75*, 745.
(108) Tennyson, J.; Zobov, N. F.; Williamson, R.; Polyansky, O. L. *J. Phys. Chem. Ref. Data* **2001**, *30*, 735.
(109) Chylek, P.; Geldart, D. J. W. *Geophys. Res. Lett.* **1997**, *24*, 2015.
(110) Fink, E. H.; Ramsay, D. A. *J. Mol. Spectrosc.* **1997**, *185*, 304.
(111) Hunziker, H. E.; Wendt, H. R. *J. Chem. Phys.* **1976**, *64*, 3488.
(112) Pushkarsky, M. B.; Zalyubovsky, S. J.; Miller, T. A. *J. Chem. Phys.* **2000**, *112*, 10695.

CR020523K